

# ScholarWorks@GSU

## Evolution of Relativistic Effects in the Photoionization of Free and Confined Heavy Atoms

Authors	Keating, David A
Citation	Keating, David A. "Evolution of Relativistic Effects in the Photoionization of Free and Confined Heavy Atoms." 2018. Dissertation, Georgia State University. <a href="https://doi.org/10.57709/12500866">https://doi.org/10.57709/12500866</a>
DOI	<a href="https://doi.org/10.57709/12500866">https://doi.org/10.57709/12500866</a>
Download date	2026-04-12 23:11:31
Link to Item	<a href="https://hdl.handle.net/20.500.14694/12248">https://hdl.handle.net/20.500.14694/12248</a>

EVOLUTION OF RELATIVISTIC EFFECTS IN THE PHOTOIONIZATION OF FREE  
AND CONFINED HEAVY ATOMS

by

DAVID KEATING

Under the Direction of Steven Manson Ph. D.

ABSTRACT

At high enough  $Z$  relativistic effects become important contributors to even the qualitative nature of atomic properties. This is likely to be true for confined atoms as well. To explore extent of relativistic effects in the photoionization of both free and confined heavy atoms, a theoretical study of the outer subshells of mercury ( $Z=80$ ), radon ( $Z=86$ ), radium ( $Z=88$ ), and nobelium ( $Z=102$ ) have been performed using the relativistic random phase approximation (RRPA) methodology in both the free and confined cases. The effects of the C60 potential modeled by a static spherical well are reasonable in the energy region well above the C60 plasmons. In order to determine which features in the photoionization cross section are due to relativistic effects, calculations using the (nonrelativistic) random phase approximation with exchange method (RPAE) are performed for comparison. It is found that relativistic interactions shift and split the nonrelativistic thresholds very considerably, and these changes in thresholds translate into very significant alterations to the nonrelativistic cross section. Relativity also alter the wave functions, contracting the s and p orbital significantly for example. These dynamic changes have considerable effects on the relativistic cross sections.

INDEX WORDS: Atomic physics, Relativistic effects, Photoionization, RRPA, RPAE, Confined atoms

EVOLUTION OF RELATIVISTIC EFFECTS IN THE PHOTOIONIZATION OF FREE  
AND CONFINED HEAVY ATOMS

by

DAVID KEATING

A Dissertation Submitted in Partial Fulfillment of the Requirements for the Degree of

Doctor of Philosophy

in the College of Arts and Sciences

Georgia State University

2018

Copyright by  
David Keating  
2018

EVOLUTION OF RELATIVISTIC EFFECTS IN THE PHOTOIONIZATION OF FREE  
AND CONFINED HEAVY ATOMS

by

DAVID KEATING

Committee Chair: Steven Manson

Committee: Vadym Apalkov

Russel White

Mukesh Dhamala

Brian Thoms

Electronic Version Approved:

Office of Graduate Studies

College of Arts and Sciences

Georgia State University

August 2018

## **DEDICATION**

This is for my wife, Michelle, and our beautiful daughters Harper and Riley, thank you for believing and supporting me through all of this.

## **ACKNOWLEDGEMENTS**

My fellow graduate students, and professors for their help and support. And Dr. Manson for guiding and putting up with me throughout this entire process.

## TABLE OF CONTENTS

<b>ACKNOWLEDGEMENTS .....</b>	<b>V</b>
<b>LIST OF TABLES .....</b>	<b>VII</b>
<b>LIST OF FIGURES .....</b>	<b>VIII</b>
<b>LIST OF ABBREVIATIONS .....</b>	<b>XIII</b>
<b>1 INTRODUCTION .....</b>	<b>1</b>
<b>2 THEORY .....</b>	<b>2</b>
<b>2.1 Photoionization.....</b>	<b>2</b>
<b>2.2 RPA Equations .....</b>	<b>5</b>
<b>2.3 Relativistic Effects.....</b>	<b>8</b>
<b>3 RESULTS AND DISCUSSION .....</b>	<b>12</b>
<b>3.1 6s and 7s Subshells .....</b>	<b>12</b>
<b>3.2 5p and 6p Subshells.....</b>	<b>21</b>
<b>3.3 5d Subshell.....</b>	<b>39</b>
<b>3.4 Confined Atoms.....</b>	<b>47</b>
<b>3.5 Threshold Shifts .....</b>	<b>49</b>
<b>3.6 Relativistic Confinement Resonances .....</b>	<b>50</b>
<b>3.7 Confinement-Affected Spin-Orbit Resonances .....</b>	<b>52</b>
<b>4 CONCLUSION .....</b>	<b>57</b>
<b>REFERENCES.....</b>	<b>58</b>

**LIST OF TABLES**

Table 1: 6s Thresholds (a.u.).....	12
Table 2: 7s Thresholds (a.u.).....	12
Table 3: 5p Thresholds (a.u.).....	21
Table 4: 4p Thresholds (a.u.).....	22
Table 5: 6p Thresholds (a.u.).....	22
Table 6: 5d Thresholds (a.u.).....	39
Table 7: Confined Thresholds (a.u.).....	49

## LIST OF FIGURES

Figure 1: The partial photoionization cross section of the 5s subshell of Xenon. ....	9
Figure 2: The partial photoionization cross section of 6s subshell of Hg, the top plot is without interchannel coupling included while the bottom one has the coupling included in the calculations. ....	13
Figure 3: The partial photoionization cross section of 6s subshell of Rn, the top plot is without interchannel coupling included while the bottom one has the coupling included in the calculations. ....	14
Figure 4: The partial photoionization cross section of 6s subshell of Ra, the top plot is without interchannel coupling included while the bottom one has the coupling included in the calculations. ....	15
Figure 5: The partial photoionization cross section of 6s subshell of Ra, the top plot is without interchannel coupling included while the bottom one has the coupling included in the calculations. ....	16
Figure 6: The partial photoionization cross section of 6s subshell of No, the top plot is without interchannel coupling included while the bottom one has the coupling included in the calculations. ....	17
Figure 7: The partial photoionization cross section of 7s subshell of Ra, the top plot is without interchannel coupling included while the bottom one has the coupling included in the calculations. ....	18
Figure 8: The partial photoionization cross section of 7s subshell of Ra, the top plot is without interchannel coupling included while the bottom one has the coupling included in the calculations. ....	19

Figure 9: The partial photoionization cross section of 7s subshell of No, the top plot is without interchannel coupling included while the bottom one has the coupling included in the calculations. ....	20
Figure 10: The partial photoionization cross section of the 5p subshell of Hg without interchannel coupling included in the calculation. ....	23
Figure 11: The partial photoionization cross section of 5p subshell of Hg, the top plot is without interchannel coupling included while the bottom one has the coupling included in the calculations. ....	24
Figure 12: The partial photoionization cross section of the 5p subshell of Rn without interchannel coupling included in the calculation. ....	25
Figure 13: The partial photoionization cross section of 5p subshell of Rn, the top plot is without interchannel coupling included while the bottom one has the coupling included in the calculations. ....	26
Figure 14 The partial photoionization cross section of the 5p subshell of Ra without interchannel coupling included in the calculation. ....	27
Figure 15: The partial photoionization cross section of 5p subshell of Ra, the top plot is without interchannel coupling included while the bottom one has the coupling included in the calculations. ....	28
Figure 16: The partial photoionization cross section of the 5p subshell of No without interchannel coupling included in the calculation. ....	29
Figure 17: The partial photoionization cross section of 5p subshell of No, the top plot is without interchannel coupling included while the bottom one has the coupling included in the calculations. ....	30

Figure 18: The partial photoionization cross section of the 6p subshell of Rn without interchannel coupling included in the calculation. ....	31
Figure 19: The partial photoionization cross section of the 6p subshell of Rn without interchannel coupling included in the calculation at higher energy. ....	31
Figure 20: The partial photoionization cross section of 6p subshell of Rn, the top plot is without interchannel coupling included while the bottom one has the coupling included in the calculations. ....	32
Figure 21: The partial photoionization cross section of 6p subshell of Rn, the top plot is without interchannel coupling included while the bottom one has the coupling included in the calculations. ....	33
Figure 22: The partial photoionization cross section of the 6p subshell of Ra without interchannel coupling included in the calculation. ....	34
Figure 23: The partial photoionization cross section of the 6p subshell of Ra without interchannel coupling included in the calculation at higher energy. ....	34
Figure 24: The partial photoionization cross section of 6p subshell of Ra, the top plot is without interchannel coupling included while the bottom one has the coupling included in the calculations. ....	35
Figure 25: The partial photoionization cross section of 6p subshell of Ra, the top plot is without interchannel coupling included while the bottom one has the coupling included in the calculations. ....	36
Figure 26: The partial photoionization cross section of the 6p subshell of No without interchannel coupling included in the calculation. ....	37

Figure 27: The partial photoionization cross section of the 6p subshell of No without interchannel coupling included in the calculation at higher energy. ....	37
Figure 28: The partial photoionization cross section of 6p subshell of Ra, the top plot is without interchannel coupling included while the bottom one has the coupling included in the calculations. ....	38
Figure 29: The partial photoionization cross section of the 5d subshell of Hg without interchannel coupling included in the calculation. ....	40
Figure 30: The partial photoionization cross section of 5d subshell of Hg. ....	41
Figure 31: The partial photoionization cross section of the 5d subshell of Rn without interchannel coupling included in the calculation. ....	42
Figure 32: The partial photoionization cross section of 5d subshell of Rn, the top plot is without interchannel coupling included while the bottom one has the coupling included in the calculations. ....	43
Figure 33: The partial photoionization cross section of the 5d subshell of Ra without interchannel coupling included in the calculation. ....	44
Figure 34: The partial photoionization cross section of 5d subshell of Ra, the top plot is without interchannel coupling included while the bottom one has the coupling included in the calculations. ....	45
Figure 35: The partial photoionization cross section of the 5d subshell of No without interchannel coupling included in the calculation. ....	45
Figure 36: The partial photoionization cross section of 5d subshell of No, the top plot is without interchannel coupling included while the bottom one has the coupling included in the calculations. ....	46

Figure 37: A@C <sub>60</sub> .....	47
Figure 38: The partial photoionization cross section of the 5p subshell of @Ra. With the RPAE 5p being plotted with a solid line, and the RRPA 5p <sub>3/2</sub> and 5p <sub>1/2</sub> with dotted and dash-dot respectively.....	51
Figure 39: The partial photoionization cross section of the total 5p subshells of @Ra. ....	52
Figure 40: The partial photoionization of the 5d subshell of both free and confined Rn, with the free case being the top plot and the confined at the bottom.....	53
Figure 41: The partial photoionization cross section of the 5d spin-orbit doublet subshells of Rn. ....	54
Figure 42: The partial photoionization of the 6p subshell of both free and confined Rn, with the free case being the top plot and the confined at the bottom.....	55
Figure 43: The partial photoionization of the 6p subshell of both free and confined Ra, with the free case being the top plot and the confined at the bottom.....	56

**LIST OF ABBREVIATIONS**

HF – Hartree-Fock

DF – Dirac-Fock

RPA – Random Phase Approximation

RPAE – Random Phase Approximation with Exchange

RRPA – Relativistic Random Phase Approximation

Xe – Xenon

Hg – Mercury

Rn – Radon

Ra – Radium

No – Nobelium

## 1 INTRODUCTION

There are several questions that arise when starting to study relativistic quantum mechanics; first of which is why even bother? Similar to the birth of non-relativistic quantum mechanics, where in the early part of the twentieth century new experiments and theoretical innovations exposed the inadequacy of the physics at the time, research in this new and mysterious quantum theory as it was at the time wasn't able to account for a number of the new phenomena without the addition of relativistic effects. These new phenomena were accounted for automatically with the introduction of the Dirac equation [1], which is the first theory to fully account for both special relativity and quantum mechanics to a rousing success. Examples of the predictions include; fine structure, spin  $-1/2$  fermions, electron spin, spin magnetic moments, and the existence of antimatter. Secondly, for more of a rational and complete reasoning, it would be very unfortunate if special relativity and quantum mechanics could not be combined. This is why, for example, there have been years and years of attempts to successfully combine general-relativity and quantum mechanics. The second, and possibly more important question is, under what circumstances will relativity significantly affect the particles? Particles become relativistic when their velocities approach the speed of light. Or when their energy is large compared to their rest mass energy. For atomic bound states, in particular, the inner s and p electrons' wavefunctions significantly contract under the influence of relativistic interactions because they travel at a significant fraction of the speed of light [2]. This relativistic contraction is more pronounced for wavefunctions with low angular momentum,  $j$ , than those with high  $j$ , and is larger for larger nuclear charge. For many-electron atoms, the contraction of the inner-shell wavefunctions screens the nucleus, altering the effective nuclear charge seen by the outer-shell wavefunctions. Due to this change in effective nuclear charge, the outer-shell wavefunctions may

either contract or expand [3]. Therefore, almost all of the elements in the periodic table experience some relativistic repercussions. These repercussions are just one of many relativistic effects that influence the atomic photoionization cross sections. It is important, and the aim of this dissertation, is to isolate and study these relativistic effects in the realm of atomic photoionization, particularly for heavy atoms. Specifically, the major motivation for this work is an attempt to understand how the combination of relativistic interactions and electron-electron correlations alter the response of heavy atoms to ionizing radiation. This is of particular importance since very heavy atoms are difficult to deal with experimentally.

## 2 THEORY

### 2.1 Photoionization

Photoionization is the process by which an electron is removed from the target by an incident photon, leaving behind an ion. Due to the fact that not all of the photons incident to a system ionize the atoms, the photoionization cross section  $\sigma_{nl}$  is a measure of the probability for ionization of an  $nl$  subshell to occur. For the derivation of the general cross section formula, the nonrelativistic equations and formulation will be used for simplicity. The relativistic structures will be discussed later in the section about the Relativistic Random Phase Approximation (RRPA). Keeping this in mind, the spin-independent (nonrelativistic) Hamiltonian describing an  $N$ -electron atom with a nuclear charge  $Z$  is as follows:

$$H = \sum_{i=1}^N \left( \frac{\mathbf{p}_i^2}{2m} - \frac{Ze^2}{r_i} \right) + \sum_{i>j=1}^N \frac{e^2}{|\mathbf{r}_i - \mathbf{r}_j|}, \quad (1)$$

where the terms in the parentheses are the kinetic and potential energy of each of the electrons in the attractive Coulomb field of the nucleus, and the last term describes the electrostatic interelectron repulsive potential energy. With  $\mathbf{p} = -i\hbar\nabla$ , the momentum operator,  $m$  is the

particle's mass,  $e$  is the charge of an electron,  $r_i$  is the position vector of the electron, and  $\hbar$  is Plank's constant. To describe the interaction with radiation additional terms are required, which can be obtained by substituting  $\mathbf{p}_i + \frac{|e|\hbar}{c}\mathbf{A}(\mathbf{r}_i, t)$  for  $p_i$  in equation 1, the resulting interaction Hamiltonian is

$$H_{int} = \sum_{i=1}^N \left[ + \frac{|e|\hbar}{2mc} (\mathbf{p}_i \cdot \mathbf{A}(\mathbf{r}_i, t) + \mathbf{A}(\mathbf{r}_i, t) \cdot \mathbf{p}_i) + \frac{e^2 \hbar^2}{2mc^2} |\mathbf{A}(\mathbf{r}_i, t)|^2 \right] \quad (2)$$

where  $\mathbf{A}(\mathbf{r}_i, t)$  is the vector potential for the incident radiation field and  $c$  is the speed of light. The  $H_{int}$  can be further simplified following the conventions and approximations laid out in [4]. First, if the vector potential is defined in the Coulomb gauge, in which  $\nabla \cdot \mathbf{A} = 0$ , then the momentum and vector potential commute which means the first two terms in equation 2 may be combined. Second, the field is treated as a perturbation so that the last term in equation 2, which is proportional to  $|\mathbf{A}|^2$ , can be dropped, which is convenient since it corresponds to two-photon processes. Third, through a so-called ‘‘happy accident’’ [5] the correct quantum-mechanical transition rate for photoionization may be calculated by treating the incident radiation classically, provided the proper amplitude for the vector potential is chosen. With this in mind, the following form was chosen:

$$\mathbf{A}(\mathbf{r}_i, t) = \left( \frac{2\pi c^2 \hbar}{\omega V} \right)^{1/2} \hat{\boldsymbol{\epsilon}} \exp(i\boldsymbol{\kappa} \cdot \mathbf{r}_i - \omega t) \quad (3)$$

where  $\boldsymbol{\kappa}$  and  $\omega$  are the wave vector and angular frequency of the incident radiation,  $\hat{\boldsymbol{\epsilon}}$  is the polarization direction, and  $V$  is the spatial volume. And finally fourth, in the electric dipole approximation the factor  $\exp(i\boldsymbol{\kappa} \cdot \mathbf{r}_i)$  is expanded as

$$\exp(i\boldsymbol{\kappa} \cdot \mathbf{r}_i) \approx 1 - i\boldsymbol{\kappa} \cdot \mathbf{r}_i + \dots \quad (4)$$

which allows an easy computation of the matrix element. Since  $\boldsymbol{\kappa} \cdot \mathbf{r} \approx \alpha/2$  in a broad region above a threshold and, since the matrix elements are squared, the expansion will be in powers of  $\alpha^2$ , the fine structure constant, i.e., a very small number. Therefore the factor  $\exp(i\boldsymbol{\kappa} \cdot \mathbf{r}_i)$  is replaced by unity, in the dipole approximation. Using these conventions and approximations and substituting equation 3 into 2, we obtain

$$H_{int} = + \frac{|e|}{mc} \left( \frac{2\pi c^2 \hbar}{\omega V} \right)^{1/2} \sum_{i=1}^N \hat{\boldsymbol{\epsilon}} \cdot \mathbf{p}_i \exp(-i\omega t). \quad (5)$$

Using  $\psi_0$  to denote the initial state of the N-electron atom, and  $\psi_k^-$  as the final state representing an outgoing photoelectron where  $k$  is the wave vector of the ionized electron, by standard procedures of time-dependent perturbation theory, the transition rate in the first order is given by [6]

$$dW_k = \frac{2\pi}{\hbar} \left| \frac{|e|}{mc} \left( \frac{2\pi c^2 \hbar}{\omega V} \right)^{1/2} \hat{\boldsymbol{\epsilon}} \cdot \langle \psi_0 | \sum_{i=1}^N \mathbf{p}_i | \psi_k^- \rangle \right|^2 \delta(E_k + E_B - \hbar\omega) k^2 dk d\Omega \quad (6)$$

where  $E_B$  is the binding energy of the ejected electron,  $d\Omega$  is an element of solid angle about the direction  $\hat{k}$ . Upon dividing the transition rate by the incident photon current density,  $c/V$  and integrating over  $dk$ , the differential photoionization cross section is obtained

$$\frac{d\sigma}{d\Omega} = \frac{4\pi^2}{\omega c} k \left( \frac{e^2}{m\hbar^2} \right) \left| \hat{\boldsymbol{\epsilon}} \cdot \langle \psi_0 | \sum_{i=1}^N \mathbf{p}_i | \psi_k^- \rangle \right|^2 \quad (7)$$

where  $\frac{\hbar^2 k^2}{2m} + E_B = \hbar\omega$  [4].

Further simplification of equation 7 requires knowledge of initial,  $\psi_0$ , and final,  $\psi_k^-$ , state wavefunctions. Due to the complexity of the atomic Hamiltonian for many-electron atoms the eigenstates must usually be obtained as linear combinations of eigenstates of a simpler model Hamiltonian using the theory of configuration interaction for the initial state wavefunctions and

the theory of scattering for the final states [4]. Due to the long-range Coulomb field, and the possible existence of many final state channels, specification of the final state is more difficult. To obtain the correct final-state wavefunction, it is required that the wavefunction describing the ionized electron to satisfy the so-called incoming wave boundary conditions; namely, at large  $r$ , the wavefunction must have the form of an outgoing plane wave plus incoming spherical waves [4].

## 2.2 RPA Equations

In the 1960's new experimental measurements of photoionization cross sections were obtained with accuracies of  $\pm 10\%$ , in the vacuum ultraviolet wavelength range [7]. It was clear that a very crucial component of atomic photoionization were electron correlations within and between the electron subshells. It was therefore necessary to move away from independent-particle, or single-channel, models such as the Hartree-Fock [8] or Dirac-Fock [9] methodologies, and towards correlated many-channel models such as the Random Phase Approximation (RPA) [10]. The RPA is historically classified as a "whole-space" correlation theory. Whole-space correlation theories are those that treat interelectron correlations numerically over the entire region of coordinate space, which focus on calculating improved wavefunctions [4]. With that in mind, the most straightforward method to include electron correlations in the final state wavefunctions is by extending the configuration-interaction procedures commonly used for bound-state problems to the continuum. The RPA is a relatively simple method for including these continuum correlation (interchannel coupling) corrections into the investigation of atomic photoionization; it yields a fully coupled, multichannel description of the photoionization process. The inclusion of these corrections is one of the key strength of the RPA methods. The RPA was originally used to describe the collective behavior of an electron

gas [4] with the phrase “random phase” being used to describe the approximation of neglecting certain matrix elements which approximately cancel each other out due to their random phases [4], in the limit of a very large number of electrons. Naturally there are difficulties with the RPA methods related to the inclusion of certain kinds of electron correlation to infinite order while ignoring other types of interactions that appear in the second and higher orders. Since only certain electron correlations are included, a Pauli principle violation arises; Amusia and Cherepkov [10] have estimated that these violations impose a limit on the accuracy of the RPA of approximately ten percent [4].

But, as the nuclear charge of the atom increases, relativistic effects become important contributors, and are needed to be included for a complete (and correct) description of the photoionization. The RPA equations are obtained by generalizing the Hartree-Fock equations,

$$\hat{H}\Psi_\varepsilon(x_1 \dots x_n) \equiv \sum_{j=1}^n \left[ \frac{-\hbar^2 \Delta_j}{2m} - \frac{Ze^2}{r_j} + \hat{U}(x_j) \right] \Psi_\varepsilon(x_1 \dots x_n) = \varepsilon \Psi_\varepsilon(x_1 \dots x_n) \quad (8)$$

where  $\hat{U}(x_j)$  is a very complicated operator, describing the direct and exchange parts of the electron-electron coulomb interaction, that depends only on the coordinate of an atomic electron and its spin [11]. Or, in the case of the relativistic random phase approximation (RRPA), the Dirac-Fock equations, which are naturally similar to the Hartree-Fock equations, except for the use of the Dirac Hamiltonian,  $h_o$ .

$$h_o = \boldsymbol{\alpha} \cdot \mathbf{p} + \beta m - \frac{Ze^2}{r}, \quad (9)$$

where  $\alpha$  and  $\beta$  are the Dirac matrices,

$$\alpha = \begin{pmatrix} 0 & \sigma \\ \sigma & 0 \end{pmatrix} \quad \beta = \begin{pmatrix} I & 0 \\ 0 & -I \end{pmatrix}, \quad (10)$$

and  $\sigma$  are the Pauli matrices

$$\sigma_x = \begin{pmatrix} 0 & 1 \\ 1 & 0 \end{pmatrix} \quad \sigma_y = \begin{pmatrix} 0 & -i \\ i & 0 \end{pmatrix} \quad \sigma_z = \begin{pmatrix} 1 & 0 \\ 0 & -1 \end{pmatrix}, \quad (11)$$

$I$  is the identity matrix, and  $\mathbf{p} = -i\nabla$  is the electron momentum operator [12] in atomic units. For the Hartree-Fock equation, the notation is borrowed from [11], while with the Dirac-Fock Hamiltonian and going forward the notation is that from [9].

The fundamental RRPA equations are obtained by expanding the Dirac-Fock (Hartree-Fock in the non-relativistic case) equations in terms of a time-dependent external field and retaining only the first-order terms leading to the eigenvalue problem [9],

$$\begin{aligned} \pm(h_o + V - \epsilon_i)w_{i\pm} \pm V_{\pm}^{(1)}u_i \mp \sum_j \lambda_{ij\pm}u_j &= \omega w_{i\pm} \\ i &= 1, 2, 3, \dots, N, \end{aligned} \quad (12)$$

where  $V$  is the Dirac-Fock potential,

$$Vu(\vec{r}) = \sum_{j=1}^N e^2 \int \frac{d^3r'}{|\vec{r}-\vec{r}'|} [(u_j^\dagger u_j)'u - (u_j^\dagger u)'u_j] \quad (13)$$

and,

$$\begin{aligned} V_{\pm}^{(1)}u_i(\vec{r}) &= \sum_{j=1}^N e^2 \int \frac{d^3r'}{|\vec{r}-\vec{r}'|} [(u_j^\dagger w_{j\pm})'u_i + (w_{j\mp}^\dagger u_j)^{''u_i} - (w_{j\mp}^\dagger u_i)^{''u_j} - \\ &(u_j^\dagger u_i)'w_{j\pm}], \end{aligned} \quad (14)$$

which includes the electron-electron correlations. The Lagrange multipliers  $\lambda_{ij\pm}$  are introduced to insure the orthogonality of the perturbed orbitals  $w_{i\pm}(r)$  to the occupied orbitals  $u_i(r)$ . The eigenvalues of the equation above provide an approximation to the excitation spectrum of the atom, including the discrete range as well as a continuum [9]. The amplitude for a transition from the ground state to the excited state described by the RRPA function  $w_{i\pm}(r)$  of frequency  $\omega$  induced by a time-dependent external field  $v_+e^{-i\omega t} + v_-e^{i\omega t}$  is given by

$$T = \sum_{i=1}^N \int d^3r (w_{i+}^\dagger v_+ u_i + w_{i-}^\dagger v_- u_i). \quad (15)$$

Extensive comparisons of the non-relativistic RPA predictions and experimental results have demonstrated that the RPA equations include most of the important correlation effects for

photoionization processes [11]. In order to calculate the photoionization cross sections, the Fortran codes from [9] for the RRPA and [11] for the RPAE are implemented, starting with the calculation of the DF orbitals and thresholds, for the relativistic cases, then using them as input to solve the RRPA equations. We calculate both the length and velocity form of the cross section to compare as a way to check the numerics of the calculations. This is possible due to the gauge invariance property of the RPA methodologies [9, 11].

### 2.3 Relativistic Effects

Relativistic effects present in atomic photoionization cross sections can be broken down into two types, static and dynamic. Static effects relate to shifts in the thresholds as compared to non-relativistic models, which isn't very important in the grand scheme of things. But in a few cases, these can bring about significant features near the threshold by pulling structures out of the discrete spectrum and into the continuum. As seen in the photoionization of Xe 5s, the Xe 5s spectrum exhibits a Cooper Minimum [13-15], it is important to take a moment to discuss the origin of these minima. Generally, both discrete and continuum states have wave functions which are oscillatory. As energy increases the continuum wavefunctions become more compact, which means its nodes move towards the nucleus. In the complicated overlap of positive and negative amplitudes which into the dipole matrix element, it may be that at some specific energy the positive and negative components cancel out giving a zero in the dipole matrix element. This is the Cooper Minimum [16].

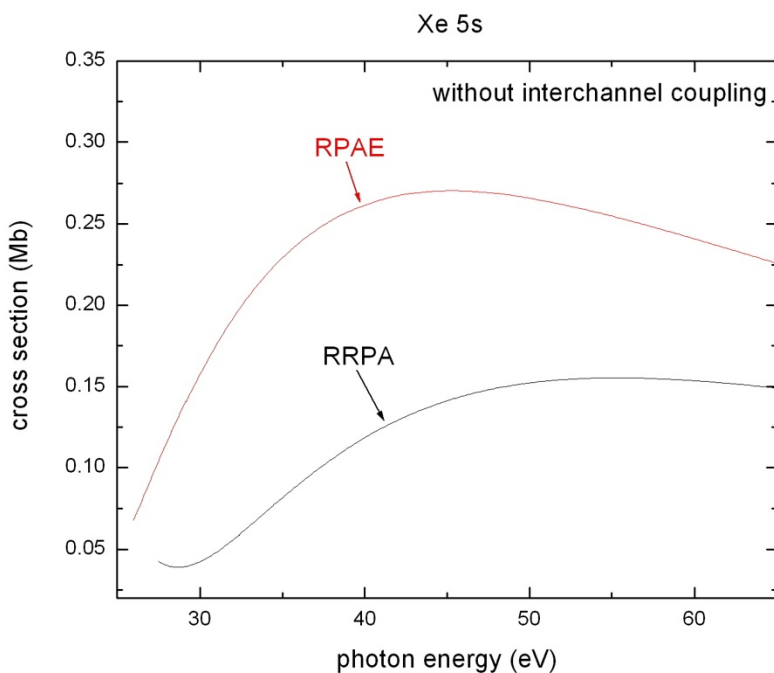


Figure 1: The partial photoionization cross section of the 5s subshell of Xenon. The black curve are the RRPA results while the red curve are the RPAE ones. Both calculations are performed without interchannel coupling included.

As seen in Figure 1, the existence of two relativistic channels in the Xe 5s threshold results in a Cooper Minimum in the continuum in the RRPA results, while in the RPAE results the minimum lies in the discrete region. Both the non-relativistic  $5s \rightarrow p$  and relativistic  $5s \rightarrow p_{3/2}$  channels have Cooper Minima in the discrete regions, while the relativistic  $5s \rightarrow p_{1/2}$  Cooper Minimum is in the continuum. Differences between relativistic and non-relativistic calculations can also result from interchannel coupling, a very important contributor to the photoionization cross section, which is a particular aspect of electron-electron correlation, and is important for most subshells of most atoms at most energies [17]. Basically what is found is that when there is a photoionization channel with a large cross section degenerate with a channel with a small cross section, interchannel coupling can modify the cross section of the channel with the smaller cross

section significantly. Electron-electron correlation in atoms and ions is a result of the Coulomb interaction between the pairs of atomic/ionic electrons [18]. The easiest static relativistic effect to observe are the splittings due to the spin-orbit interaction, which becomes significant at high  $Z$ , but can be seen across the periodic table and should be considered in all cases. The existence of the spin-orbit splitting has a measurable effect on Cooper minima in the photoionization cross section, as seen in Figure 1, and was the explanation of why the Cooper minima were found to be broader and shallower than was predicted using non-relativistic models [19].

The dynamic effects relate to changes in the wavefunctions due to relativistic and interchannel interactions, which are more difficult to accurately pick out and cannot be replicated in non-relativistic models like the static effects. In order to examine the dynamic effects on the cross section it is useful to recalculate the partial cross sections without the inclusion of interchannel coupling and to plot them with respect to photoelectron energy rather than photon energy, and compare to the artificially created partial cross sections of the spin-orbit doublet subshells from a non-relativistic model. This removes the static effects and any induced effects due to interchannel coupling. Any discrepancies between the two models must be a result of dynamic relativistic effects. Both static and dynamic effects combine with interchannel coupling to produce spin-orbit activated interchannel coupling, which is a purely relativistic effect. Interchannel coupling between channels arising from the two spin-orbit substates engendered owing to the spin-orbit interaction breaking the degeneracy among the electrons of a subshell. This effect was first discovered experimentally [20] in the photoionization of the the 3d subshell of Xe, where the  $3d_{5/2}$  cross section was found to exhibit an extra resonance-like behavior just above the  $3d_{3/2}$  threshold. This behavior was explained [21] as resulting from the interchannel coupling between the  $3d_{3/2} \rightarrow f$  channels, which have a significant shape resonance just above the

$3d_{3/2}$  threshold, with the  $3d_{5/2} \rightarrow f$  channels, thereby yielding the resonance-like structure in the  $3d_{5/2}$  photoionization cross section. This phenomenon was termed spin-orbit activated interchannel coupling [21]. The phenomenon was also exhibited in photoelectron angular distribution parameters, both dipole [22] and quadrupole [23], and was confirmed to exist in other atoms as well, both experimentally and theoretically [24-28]. Based upon our understanding from these works, it is expected that spin-orbit activated interchannel coupling will lead to new structures in the photoionization of any pair of spin-orbit split channels containing near-threshold shape resonances. It is the aim of this paper to isolate these relativistic effects and explore how they evolve as  $Z$  increases. This will be accomplished by calculating the cross sections of heavy atoms using both the RRPA and its non-relativistic counterpart RPAE. Since both of these models are based on the RPA methodology, other than relativistic effects, both models assume the same approximations, thereby allowing us to accurately isolate and label the changes in the cross sections due to relativistic effects. To explore how these relativistic effects evolve as  $Z$  increases, the results will be arranged *via* subshell rather than element, starting with examining the changes in thresholds, then looking at partial cross sections without interchannel coupling and plotted versus photoelectron energy, followed by comparisons without interchannel coupling but plotted against photon energy, and finally putting interchannel coupling back into the calculations, basically building up to a complete relativistic calculation. We include in our study the outer subshells of mercury ( $Z = 80$ ), radon ( $Z = 86$ ), radium ( $Z = 88$ ), and nobelium ( $Z = 102$ ) as representative atoms. These systems were chosen because they are the heaviest closed-shell atoms. As such, we expect relativistic effects to be more pronounced and therefore easier to identify.

### 3 RESULTS AND DISCUSSION

#### 3.1 6s and 7s Subshells

The  $ns$  subshells are chosen to study first because they do not form a spin-orbit doublet under the action of relativistic effects, which simplifies the study of the dynamic effects. The 6s and 7s subshell thresholds are presented below starting with the 6s, which is the valance subshell of mercury, making those results different from the other elements' 6s results, and more in line with the 7s results of radium and nobelium. They are presented here for simplicity but will be discussed in connection with the 7s subshells. All the energies are presented in atomic units (a.u.) in Table 1.

Table 1: 6s Thresholds (a.u.)

Element	Hg	Rn	Ra	No
HF	0.26	0.87	1.37	1.89
DF	0.33	1.07	1.62	2.81

Looking at Table 1, there is a clear pattern present: as the nuclear charge increases so does the difference between the DF and HF thresholds. The 6s wavefunction contracts, as the nuclear charge increases, so that the 6s subshell becomes more bound therefore taking more photon energy to excite it, which is what is shown in Table 1. Due to the shielding of the nucleus by the inner subshells, the 7s (Table 2) wavefuctions experience the least amount of contraction of all the  $ns$  subshells. Compared to the 6s thresholds in Table 1, the difference between the relativistic and non-relativistic thresholds are negligible. Once again the energies are presented in atomic units (a.u.)

Table 2: 7s Thresholds (a.u.)

Element	Ra	No
HF	0.15	0.17
DF	0.17	0.21

As expected, as the nuclear charge increases the separation between the HF and DF thresholds increases, as seen in Table 2. Due to the relativistic contractions in the  $ns$  wavefunctions, the  $ns$  electrons are more bound than their non-relativistic counterparts, which is why all of the DF energies for the  $ns$  subshells are larger than the corresponding HF ones.

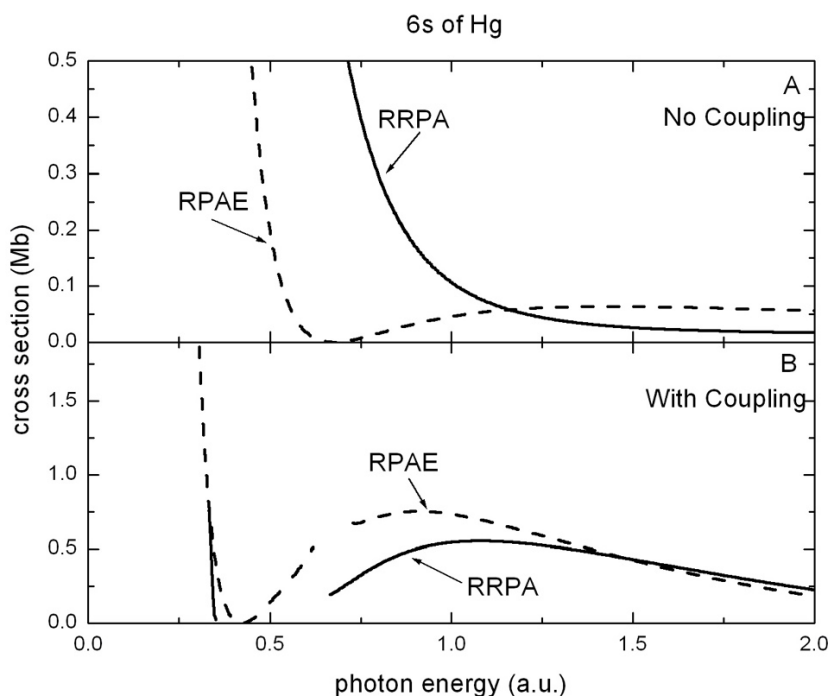


Figure 2: The partial photoionization cross section of 6s subshell of Hg, the top plot is without interchannel coupling included while the bottom one has the coupling included in the calculations. In both plots the solid curve is the RPAE results and the dashed are the RRPA 6s. Since interchannel coupling is included in the bottom calculations resonances due to opening channels are present, and this region, below the 5d thresholds, is omitted in the lower panel.

It is useful to compare the cross sections of the two models without the inclusion of interchannel coupling because, normally, the interaction with nearby subshells overshadow the 6s cross section, in particular the proximity of the 5d subshells. There is a clear difference between the RPAE and RRPA uncoupled results in the top plot in Figure 2, which is the absence of the Cooper Minimum in the RRPA cross section. As the nuclear charge increases, in the RPAE cross section, the Cooper Minimum falls into the discrete spectrum (See the top plots of Figures 3, 4,

and 5). Studying the descent of the minimum into the discrete reveals that the Cooper Minimum is absent from the RRPA cross section and not just in the discrete spectrum. Coupling with the 5d channels enhances the minima in the RPAE cross section and induces one in the RRPA cross section, as seen in the bottom plot of Figure 2. The discontinuity in the RRPA curve in the bottom plot of Figure 2 is due to the omission of the resonances due to the opening of the 5d channels. The inclusion of interchannel coupling brings the two models into better agreement. This is because of the similarity between the 5d cross sections, which isn't greatly affected by relativity as will be seen below in our study of the 5d subshell cross section.

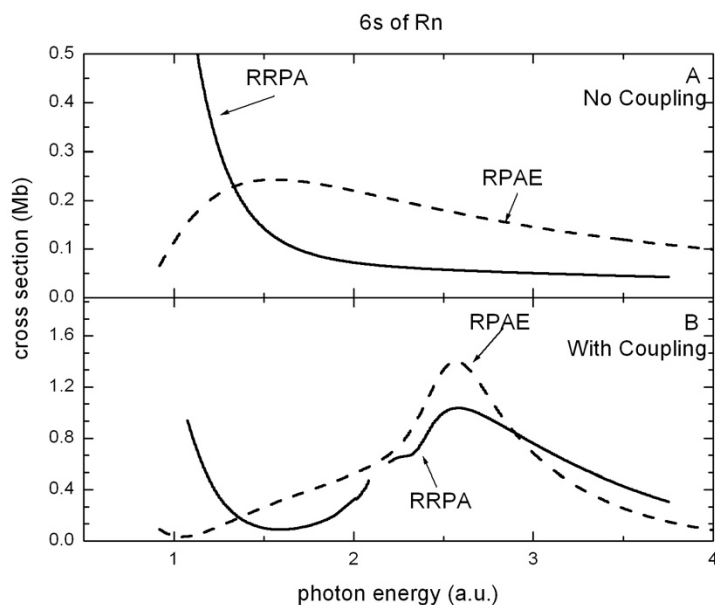


Figure 3: The partial photoionization cross section of 6s subshell of Rn, the top plot is without interchannel coupling included while the bottom one has the coupling included in the calculations. In both plots the solid curve is the RPAE results and the dashed are the RRPA 6s. Since interchannel coupling is included in the bottom calculations resonances due to opening channels are present, and this region, below the 5d threshold, is omitted.

Just as in the bottom plot of Figure 2, interchannel coupling pulls the Cooper Minimum out of the discrete spectrum in the RPAE cross section for Rn, shown in Figure 3. In the RRPA cross section once again there is an induced minimum. There is even evidence of the spin-orbit

activated resonance present from the interaction with the 5d (see Figure 35) cross section that is transferred to the 6s cross section *via* interchannel coupling.

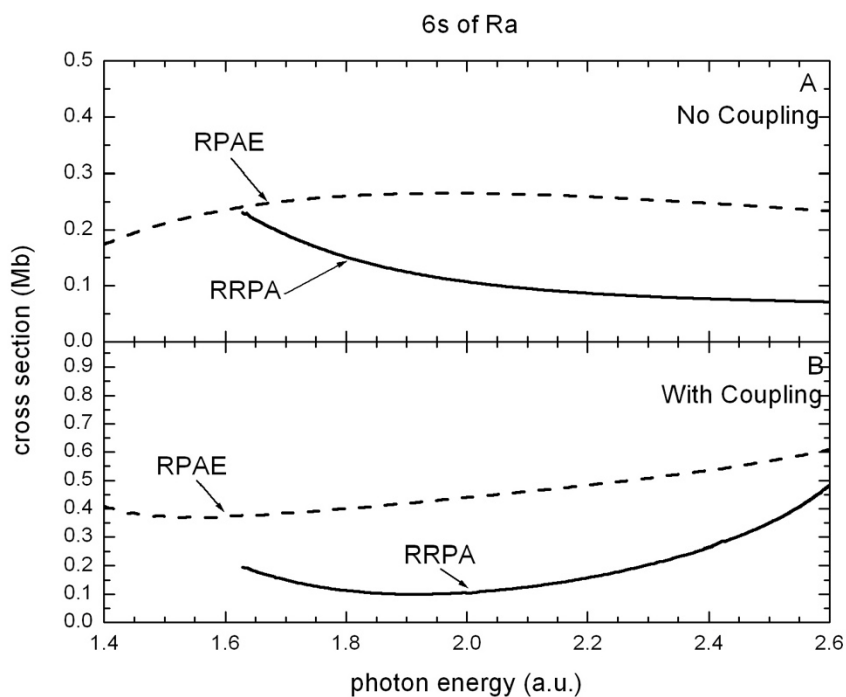


Figure 4: The partial photoionization cross section of 6s subshell of Ra, the top plot is without interchannel coupling included while the bottom one has the coupling included in the calculations. In both plots the solid curve is the RPAE results and the dashed are the RRPA 6s.

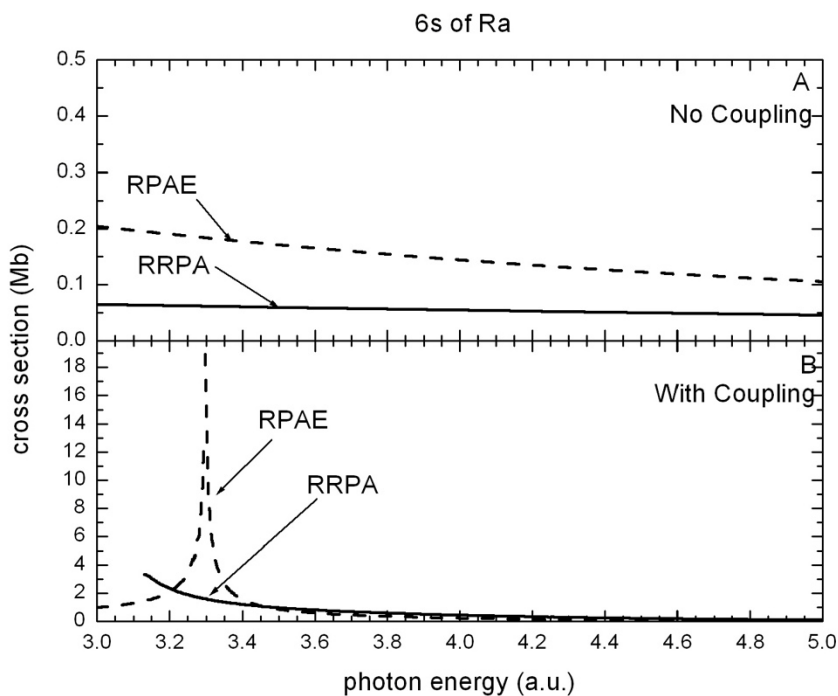


Figure 5: The partial photoionization cross section of 6s subshell of Ra, the top plot is without interchannel coupling included while the bottom one has the coupling included in the calculations.

In both plots the solid curve is the RPAE results and the dashed are the RRPA 6s.

Figures 4 and 5, for Ra, continues the trend of the minima falling into the discrete. Like in radon (Figure 3) the inclusion of interchannel coupling pulls the minima out of the discrete spectrum although it is less significant here. It is of interest that, while both calculations experience a noticeable discontinuity at the opening of the 5d thresholds, the RPAE sees a greater jump at the opening of the 5d subshell at about  $3.3 \text{ a.u.}$  in the bottom plot of Figure 5.

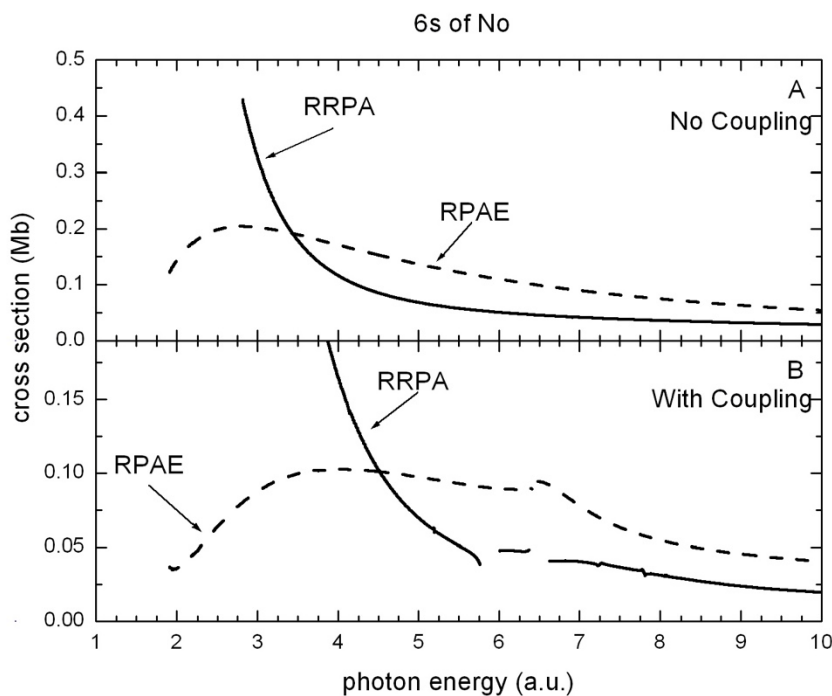


Figure 6: The partial photoionization cross section of 6s subshell of No, the top plot is without interchannel coupling included while the bottom one has the coupling included in the calculations. In both plots the solid curve is the RPAE results and the dashed are the RRPA 6s. Since interchannel coupling is included in the bottom calculations resonances due to opening channels are present, and the gaps are the resonance regions which are omitted.

In the bottom plot of Figure 6, for No, there is no induced minimum in the RRPA curve, unlike the other cases. This is due to the fact that the effect of the 5d cross section of nobelium (Figure 39), *via* interchannel coupling, is far less than the other 5d cross sections, because the 5d threshold is considerably further away from the 6s in nobelium than the other cases.

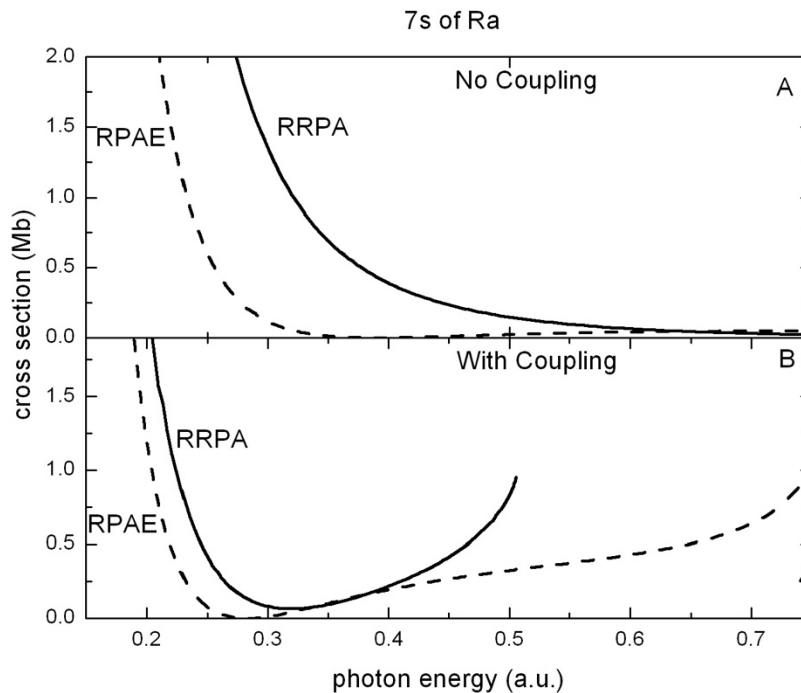


Figure 7: The partial photoionization cross section of 7s subshell of Ra, the top plot is without interchannel coupling included while the bottom one has the coupling included in the calculations.

In both plots the solid curve is the RPAE results and the dashed are the RRPA 7s.

Just as in the 6s case of mercury, Figure 2, in the top plot (without coupling) the RPAE cross section, for Ra, Figure 7, has a distinct Cooper Minimum, whereas the RRPA cross section does not have a Cooper Minimum. This missing minimum completely changes the cross section, the Cooper Minimum is easier to see in the top plot of Figure 8. With the inclusion of interchannel coupling, a Cooper Minimum is induced in the RRPA cross section, see in the bottom plot of Figure 7.

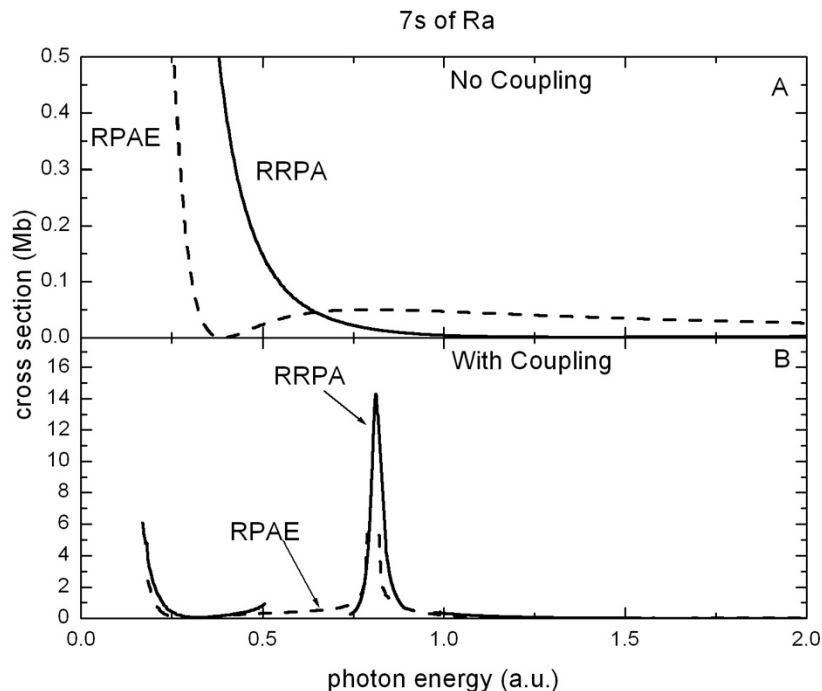


Figure 8: The partial photoionization cross section of 7s subshell of Ra, the top plot is without interchannel coupling included while the bottom one has the coupling included in the calculations. In both plots the solid curve is the RPAE results and the dashed are the RRPA 7s. Since interchannel coupling is included in the bottom calculations resonances due to opening channels are present, and the gaps are the resonance regions which are omitted.

The introduction of interchannel coupling with the  $6p_{3/2}$  and  $6p_{1/2}$  subshells brings the two models into better agreement since the coupling dominates the cross section, seen in the bottom plot of Figure 8. The resonance in the RRPA results, at around  $0.75 \text{ a.u.}$ , is clearly induced by interchannel coupling with the 6p subshells since there is no hint of it without coupling included. The coupling with the 6p cross sections of radium induce the similarities found in the 7s cross section with coupling. The 7s cross section of nobelium is very similar to the radium 7s case, as seen in the Figure 9.

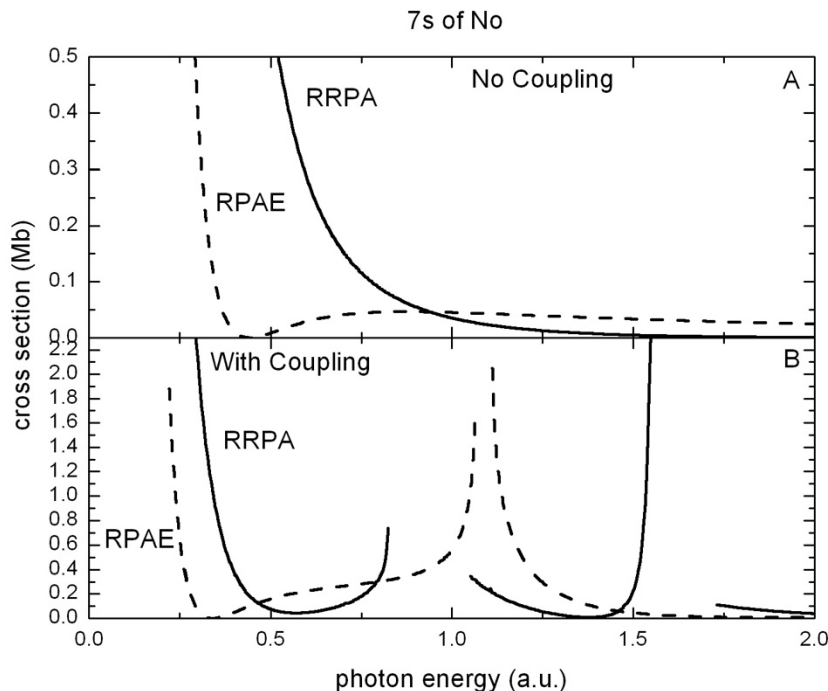


Figure 9: The partial photoionization cross section of 7s subshell of No, the top plot is without interchannel coupling included while the bottom one has the coupling included in the calculations. In both plots the solid curve is the RPAA results and the dashed are the RRPA 7s. Since interchannel coupling is included in the bottom calculations resonances due to opening channels are present, and the resonance regions are omitted causing the gaps.

In the bottom plot of Figure 9, the inclusion of interchannel coupling doesn't bring the two models into better agreement like in the other  $ns$  cross sections. This is due to the different thresholds of the 6p subshells between the two models. Although this only creates a slight disagreement, it is still important to note. Also due to the increased separation between the 7s and 6p thresholds in nobelium, compared to the separation in radium, the near threshold behavior of the cross section is retained, due to the decreased effect of interchannel coupling with the 6p channels. The gaps in the RRPA and RPAA results are the resonance region near the opening of the 6p subshells, which have been removed.

Relativistic effects completely eliminate the 6s Cooper Minimum found in the non-relativistic cross sections. This significantly changes the cross section making them completely

different. In both the 6s and 7s cross sections, the inclusion of interchannel coupling diminishes the dynamic effects, because the cross sections of the surrounding subshells will overshadow the  $ns$  cross sections. Interchannel coupling with the 5d included in the 6s cross sections gives the two models similarity because the two models' 5d cross section are very similar. Both of the 7s cross sections are practically the same and are similar to the 6s cross section of mercury, because all of them are valence subshells for their respective atoms. Once again the dynamic effects are diminished by the inclusion of interchannel coupling with the 6p subshells.

### 3.2 5p and 6p Subshells

The respective 5p thresholds for each element in the investigation are displayed in Table 3 below. All of the energies are presented in atomic units (a.u.), and the DF\* column refers to the  $l - \frac{1}{2}$  ( $5p_{1/2}$ ) thresholds while the un-starred DF refers to the  $l + \frac{1}{2}$  ( $5p_{3/2}$ ).

Table 3: 5p Thresholds (a.u.)

Element	Hg	Rn	Ra	No
HF	2.85	5.23	6.45	11.01
DF	2.84	5.21	6.37	11.43
DF*	3.54	6.41	7.84	15.55

Looking at the difference between the un-starred DF and HF thresholds, which are quite similar, as  $Z$  increases so does the relative difference. This increase is what is expected because relativistic effects should increase as  $Z$  does. But these differences are not very significant until we reach nobelium with a difference of  $0.42$  a.u., which is  $11.43$  eV, to put in perspective.

Comparing the DF\* thresholds with the HF, there are more dramatic changes, which also increase with  $Z$ . This is expected as the  $p_{1/2}$  subshells act more like  $s$  subshells at high  $Z$  and are, therefore, more compact. The anomaly is the nobelium un-starred DF threshold which is larger than its HF counterpart, which is the opposite of the other three cases. This is because in nobelium the 5p is deeper than the other cases, and behaves more like the respective 4p

thresholds, Table 4, where all of the un-starred DF thresholds are at higher energies compared to their HF counterparts.

Table 4: 4p Thresholds (a.u.)

Element	Hg	Rn	Ra	No
HF	21.70	29.49	32.72	53.01
DF	22.19	30.12	33.40	55.20
DF*	26.12	36.02	40.12	70.99

With respect to the 4p threshold there is no outlier and everything behaves as expected. For outer and near outer subshell electrons, the un-starred DF energies are lower than the respective HF energies, while for inner subshells, the reverse is true; this is due to the amount of shielding the inner subshells have on the effective nucleus charge causing the outer electrons to become less bound. This shielding is due to inner subshells contracting or expanding due to relativity. As, for example, the 1s electron contracts it shields the outer electrons more effectively from the nucleus. This effect is evident in the 6p thresholds, Table 5

Table 5: 6p Thresholds (a.u.)

Element	Rn	Ra	No
HF	0.43	0.82	1.11
DF	0.38	0.74	1.05
DF*	0.54	0.97	1.73

Just as in Table 3, the differences between the un-starred DF and HF thresholds increases as the nuclear charge increases. And there are more drastic changes when comparing the DF\* and HF thresholds. That being said, neither of these changes are very significant, which is expected as the 6p subshell is the valance subshell in radon and the second most outer subshell in radium and nobelium. All of the inner subshells are shielding the nucleus, partially negating the effects of the 6p wavefunction contraction due to relativity, which is why the un-starred DF thresholds are less bound than the HF thresholds, and the difference between the DF\* and HF thresholds is not as significant as the 5p thresholds in Table 3. Speaking of dynamic effects, looking at the 5p

photoionization cross section of mercury, it is clear that the effect of changes in the wavefunctions is more important than the altered thresholds.

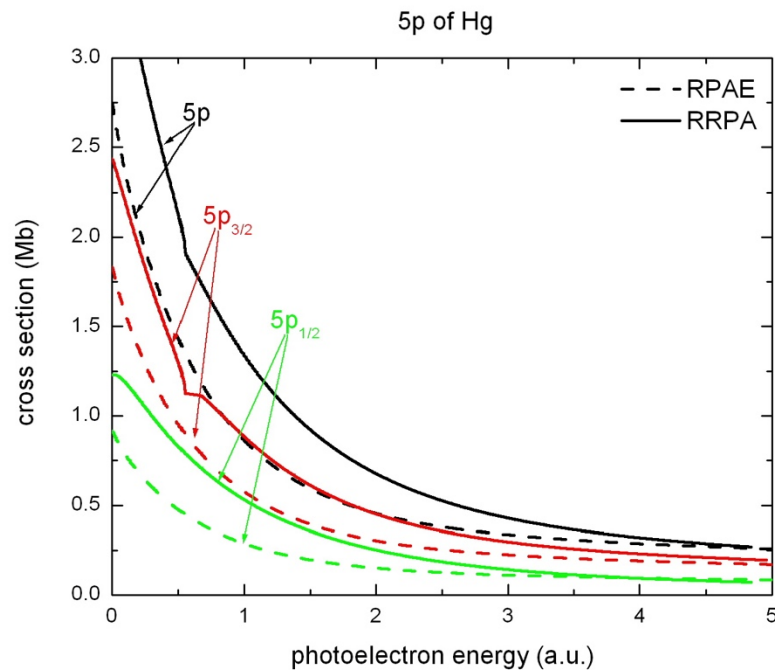


Figure 10: The partial photoionization cross section of the 5p subshell of Hg without interchannel coupling included in the calculation.

The solid curves are the results of the RRPA calculations while the dashed curves are the RPAE results. The RPAE  $5p_{3/2}$  and  $p_{1/2}$  are produced by taking the normal RPAE result and multiplying by the corresponding branching ratios. The kink in the RRPA  $5p_{3/2}$  plot is due to the removal of the resonances of the  $5p_{1/2}$  channel opening up. The  $5p$  total is the summation of the  $5p_{3/2}$  and  $5p_{1/2}$  channels.

Figure 10 is plotted against photoelectron energy to remove the effects of the shifted thresholds, in order to study the dynamic effects. To explore these effects on the individual spin-orbit channels, the nonrelativistic RPAE result is multiplied by the corresponding branching ratios; these between  $j = l + \frac{1}{2}$ , and  $j = l - \frac{1}{2}$  subshells would be  $\frac{l+1}{2l+1}$  and  $\frac{l}{2l+1}$  respectively, in the absence of relativistic effects [28]. Comparing the solid and dashed lines, all of the discrepancies are the result of dynamic effects on the subshell. These effects fall off as the energy increases

away from threshold. Amazingly, the RRPA  $5p_{3/2}$  channel alone is practically equal to the total RPAE cross section after the  $5p_{1/2}$  threshold. Plotting against photon energy will add back in, the effect of the shifted threshold. Looking at the RRPA curves, there is a slight impression of a maximum that isn't present in the RPAE curves; it is easier to see in Figure 11.

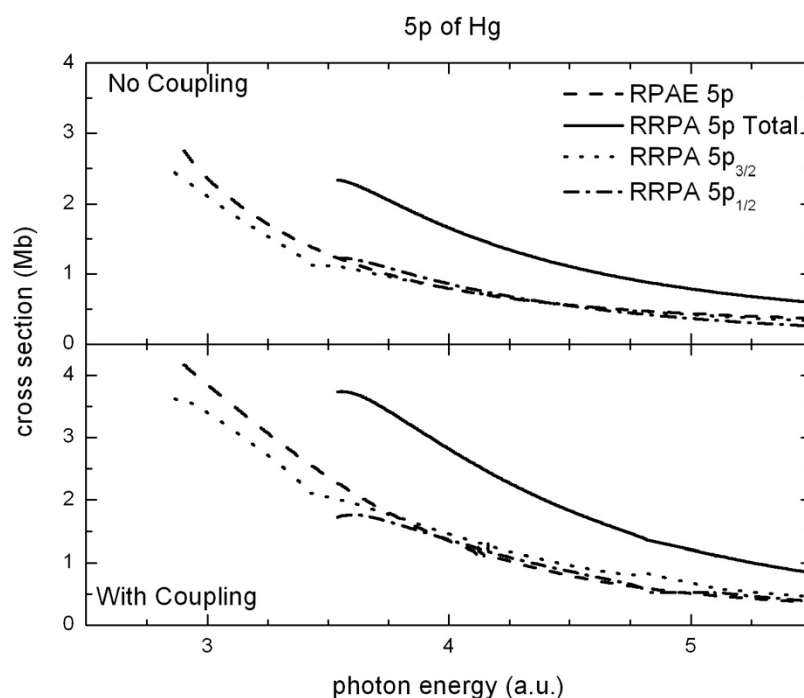


Figure 11: The partial photoionization cross section of 5p subshell of Hg, the top plot is without interchannel coupling included while the bottom one has the coupling included in the calculations. In both plots the dashed curve is the RPAE results and the dotted, dash-dot, and solid are the RRPA  $5p_{3/2}$ ,  $5p_{1/2}$ , and 5p total respectively.

With the shifted thresholds back in play is easier to observe the magnitude of the RRPA  $5p_{3/2}$  cross section which in the top plot is practically equal to the RPAE 5p cross section after the opening of the  $5p_{1/2}$  threshold. Speaking of the  $5p_{1/2}$  cross section, at threshold it is equal to the RPAE and greater than, slightly, the  $5p_{3/2}$  cross section. The addition of interchannel coupling, of the 5d channels, enhances the impression of the maximum that was seen in Figure 10.

Interchannel coupling introduces several little effects, such as increases the overall magnitude of

all of the cross sections. The  $5p_{3/2}$  becomes greater than the RPAE, rather than equaling it, going into the  $5s$  threshold region. The  $5p_{1/2}$  at threshold is significantly less than the RPAE but, like the  $5p_{3/2}$ , crosses it as energy increases. These changes are interesting but not that significant. In the  $5p$  cross section of mercury the most important effects are clearly the dynamic effects.

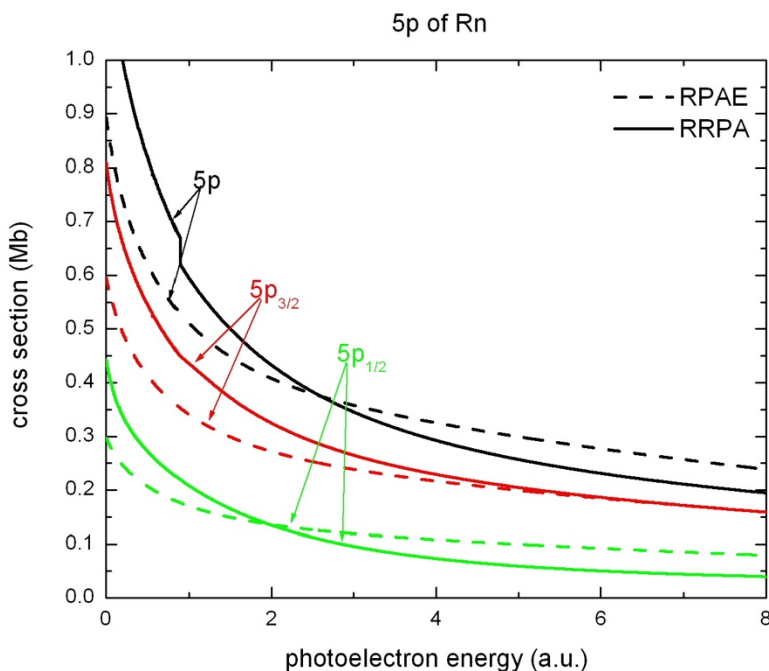


Figure 12: The partial photoionization cross section of the  $5p$  subshell of Rn without interchannel coupling included in the calculation.

The solid curves are the results of the RRPA calculations while the dashed curves are the RPAE results. The RPAE  $5p_{3/2}$  and  $p_{1/2}$  are produced by taking the normal RPAE result and multiplying by the corresponding branching ratios. The kink in the RRPA  $5p_{3/2}$  plot is due to the removal of the resonances of the  $5p_{1/2}$  channel opening up. The  $5p$  total is the summation of the  $5p_{3/2}$  and  $5p_{1/2}$  channels.

Just as in Figure 10, Figure 12, for Rn, is plotted against photoelectron energy for the same reasons. The differences between the dashed and the solid curves are similar in magnitude to the mercury  $5p$  cross sections. Unlike that case, however, the  $5p_{1/2}$  curves do not converge as energy increases and, in fact, appear to diverge as energy increases. The  $5p_{3/2}$  cross sections also do converge as they did in the mercury  $5p$  case. This difference in behavior of the two spin-orbit

channels explains the behavior of the total cross sections. Figure 10 implies that dynamic effects affect the  $5p_{1/2}$  channel more than the  $5p_{3/2}$ ; at this point it is impossible to declare if this is a general effect or occurs just in this case.

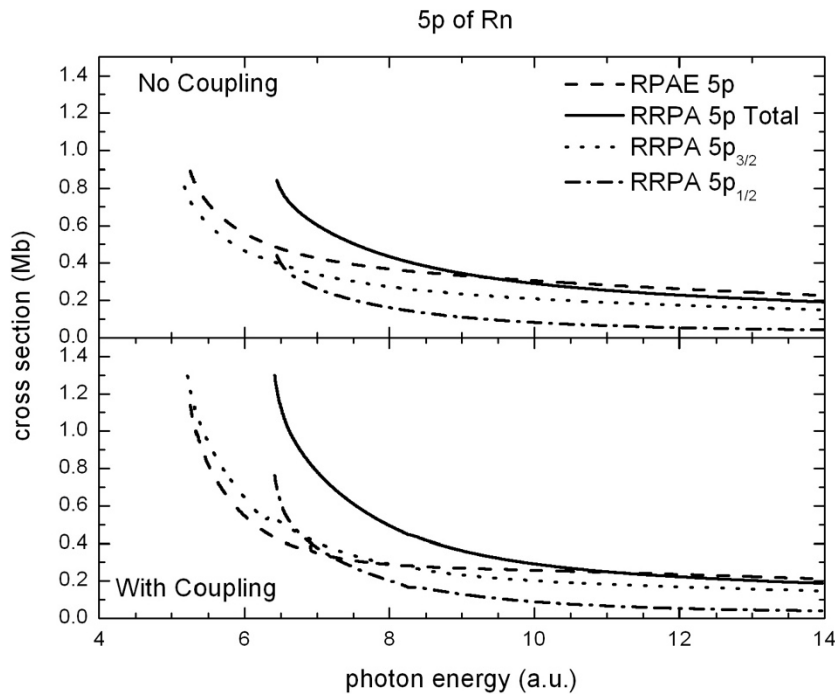


Figure 13: The partial photoionization cross section of 5p subshell of Rn, the top plot is without interchannel coupling included while the bottom one has the coupling included in the calculations. In both plots the dashed curve is the RPAE results and the dotted, dash-dot, and solid are the RRPA  $5p_{3/2}$ ,  $5p_{1/2}$ , and 5p total respectively.

Comparing the behavior of the  $5p_{1/2}$  cross sections of radon and mercury, without coupling included, at threshold in Rn is greater than the  $5p_{3/2}$  like in mercury, but below the RPAE cross section. And then it quickly falls off more rapidly than in mercury. Unlike the mercury  $5p_{3/2}$ , the radon one is never equal to the RPAE cross section. Once again, with the introduction of interchannel coupling, with the 5d channels, the overall magnitude of the cross sections is increased; both of the spin-orbit channels have greater amplitudes at their respective thresholds, with the  $5p_{1/2}$  amplitude being greater than the  $5p_{3/2}$  cross section. But just as in the top plot of

Figure 13, the spin-orbit cross sections fall below the RPAE as energy increases. Interchannel coupling has greater effects on the cross sections in Rn, when compared to mercury, while dynamic effects are less important.

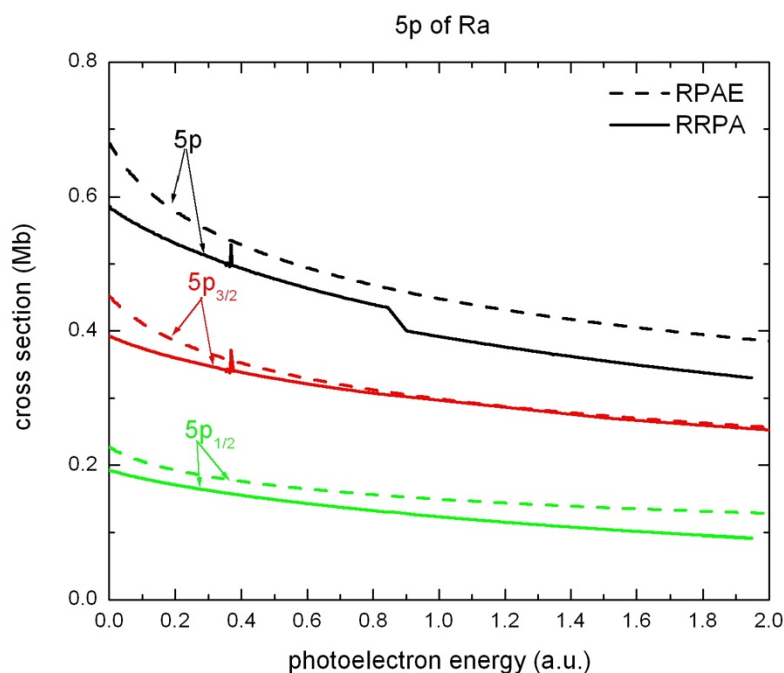


Figure 14 The partial photoionization cross section of the 5p subshell of Ra without interchannel coupling included in the calculation. The solid curves are the results of the RRPA calculations while the dashed curves are the RPAE results. The RPAE  $5p_{3/2}$  and  $p_{1/2}$  are produced by taking the normal RPAE result and multiplying by the corresponding branching ratios. The kink in the RRPA  $5p_{3/2}$  plot is due to the removal of the resonances of the  $5p_{1/2}$  channel opening up. The  $5p$  total is the summation of the  $5p_{3/2}$  and  $5p_{1/2}$  channels.

Continuing the trend established in Figure 12, the differences between the dashed and solid curves decreases for Ra, Figure 14. Of course it is expected for radon and radium to be affected by relativity in very similar ways, because radium's nuclear charge ( $Z = 88$ ) is only two greater than radon's nuclear charge ( $Z = 86$ ). Once again the  $5p_{3/2}$  curves converge rather quickly while

the  $5p_{1/2}$  curves diverge increasingly with energy, just as in Figure 12 for radon, lending more weight to this phenomenon being a general occurrence.

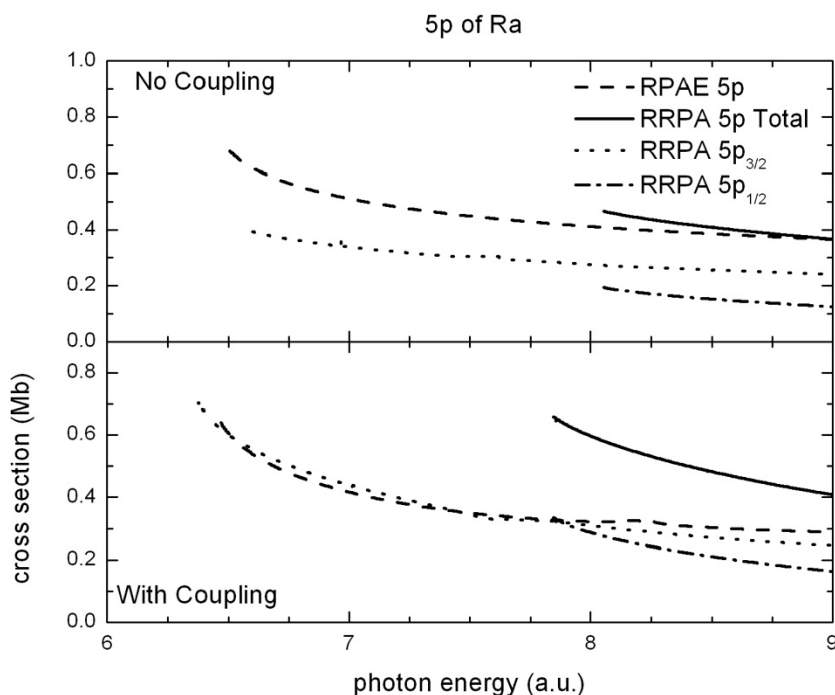


Figure 15: The partial photoionization cross section of 5p subshell of Ra, the top plot is without interchannel coupling included while the bottom one has the coupling included in the calculations. In both plots the dashed curve is the RPAE results and the dotted, dash-dot, and solid are the RRPA  $5p_{3/2}$ ,  $5p_{1/2}$ , and 5p total respectively.

In the top plot of Figure 15, the dynamic effects, for Ra, are diminished by the shifted thresholds.

It appears that as nuclear charge increases, relativistic effects decrease in the cases without coupling, as seen in the top plots of Figure 11, 13, and 15. This is due to the fact that, with increasing nuclear charge, the 5p subshell moves deeper into the atom from being an outer shell, as in mercury, and more into the inner-middle subshells. This changes the amount of shielding of the nucleus by the inner subshells, therefore changing the strength of the dynamic effects. The effects of interchannel coupling also has decreased; they decreased in radon as well but wasn't noted. This is due to increasing difference between the 5d and the 5p thresholds. The further

away from the threshold, the lower the magnitude of the 5d cross sections. So, as the 5p thresholds become further and further away from the 5d ones, the less of an effect the coupling with the 5d channels becomes. The addition of interchannel coupling of the 5d channels brings similar effects as it did in radon, but less impressive this time around. This trend continues in the cross sections of nobelium.

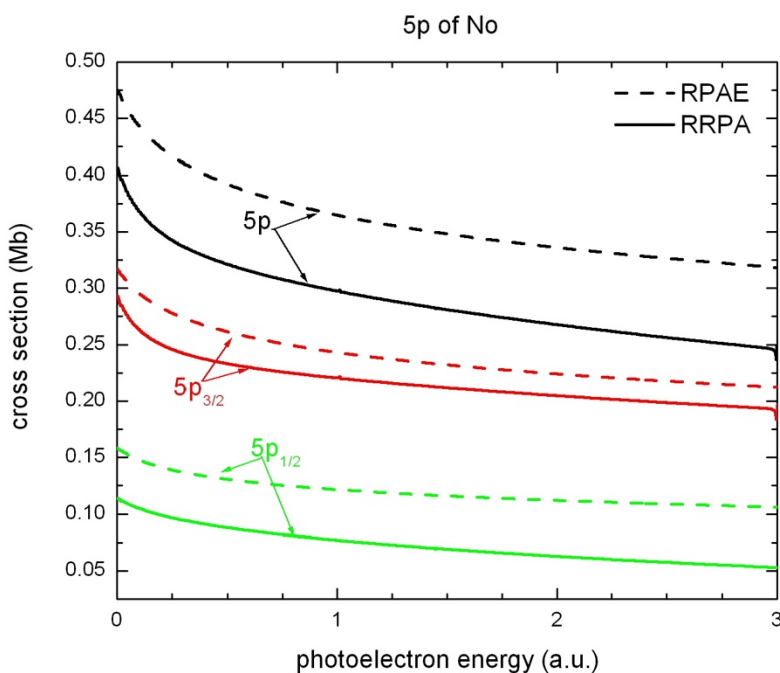


Figure 16: The partial photoionization cross section of the 5p subshell of No without interchannel coupling included in the calculation.

The solid curves are the results of the RRPA calculations while the dashed curves are the RPAE results. The RPAE  $5p_{3/2}$  and  $p_{1/2}$  are produced by taking the normal RPAE result and multiplying by the corresponding branching ratios. The kink in the RRPA  $5p_{3/2}$  plot is due to the removal of the resonances of the  $5p_{1/2}$  channel opening up. The 5p total is the summation of the  $5p_{3/2}$  and  $5p_{1/2}$  channels.

Compared to Figure 10, the dynamic effects, in No 5p, Figure 16, have diminished at threshold, as compared to radon and radium, given that the  $5p_{3/2}$  curves don't converge. Also the trend continues of dynamic effects having a  $j$  dependence as the  $5p_{1/2}$  curves diverge once more, as

energy increases. To establish if this is a general pattern in the 5p cross sections, investigation into the 6p cross sections will determine if this is shared with the other  $p$  subshells.

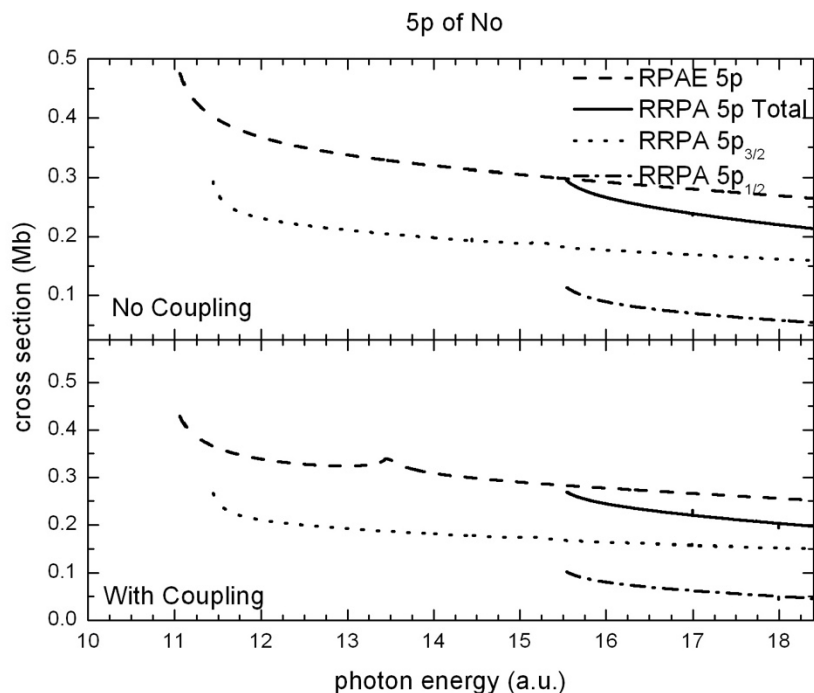


Figure 17: The partial photoionization cross section of 5p subshell of No, the top plot is without interchannel coupling included while the bottom one has the coupling included in the calculations. In both plots the dashed curve is the RPAE results and the dotted, dash-dot, and solid are the RRPA  $5p_{3/2}$ ,  $5p_{1/2}$ , and 5p total respectively.

The top plot of Figure 17 continues the trend from the top plot of Figure 15, this time even the RRPA 5p total is below the RPAE cross section. Unlike the previous three cases, the introduction of interchannel coupling decreases the overall magnitudes of the cross sections. There are very insignificant changes added by the interchannel coupling of the 5d channels; this is explained above in the discussion of Figure 16.

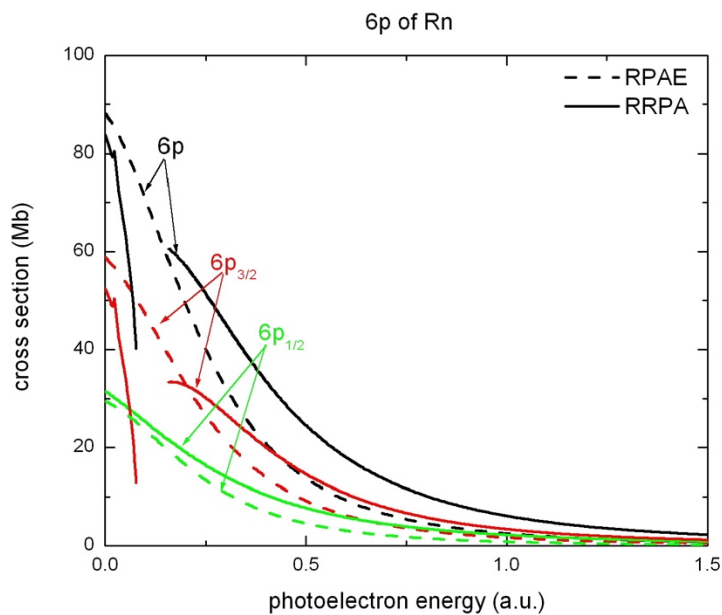


Figure 18: The partial photoionization cross section of the 6p subshell of Rn without interchannel coupling included in the calculation.

The solid curves are the results of the RRPA calculations while the dashed curves are the RPAE results. The RPAE  $6p_{3/2}$  and  $6p_{1/2}$  are produced by taking the normal RPAE result and multiplying by the corresponding branching ratios.

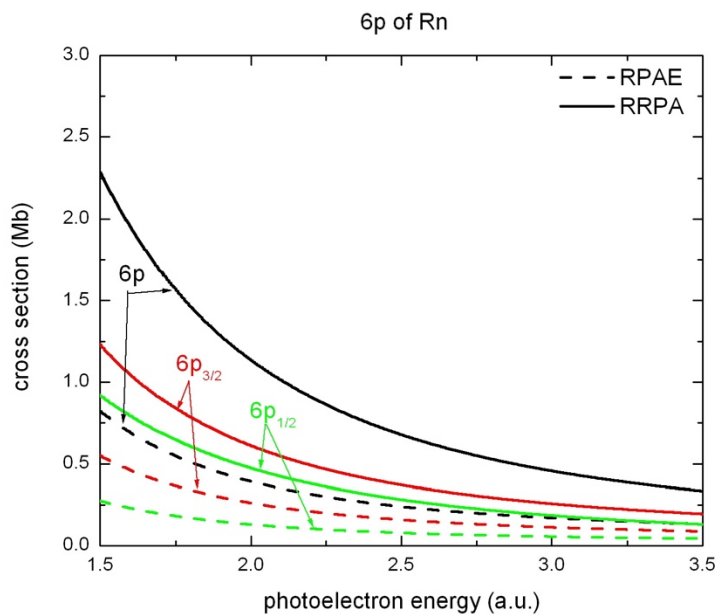


Figure 19: The partial photoionization cross section of the 6p subshell of Rn without interchannel coupling included in the calculation at higher energy.

The solid curves are the results of the RRPA calculations while the dashed curves are the RPAE results. The RPAE  $6p_{3/2}$  and  $6p_{1/2}$  are produced by taking the normal RPAE result and multiplying by the corresponding branching ratios.

Both Figure 18 and 19 present the dynamic effects in the  $6p$  cross sections of radon. Near the threshold, Figure 18, the dynamic effects cause the RRPA cross sections to have greater magnitudes than the RPAE. This is seen to continue as photoelectron energy increases, with even greater differences between the curves.

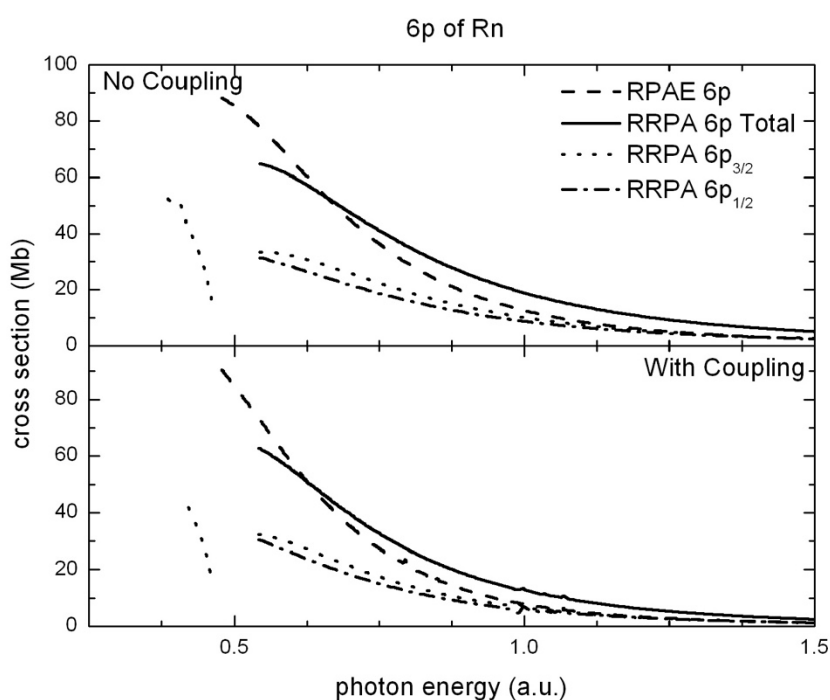


Figure 20: The partial photoionization cross section of  $6p$  subshell of Rn, the top plot is without interchannel coupling included while the bottom one has the coupling included in the calculations. In both plots the dashed curve is the RPAE results and the dotted, dash-dot, and solid are the RRPA  $6p_{3/2}$ ,  $6p_{1/2}$ , and  $6p$  total respectively.

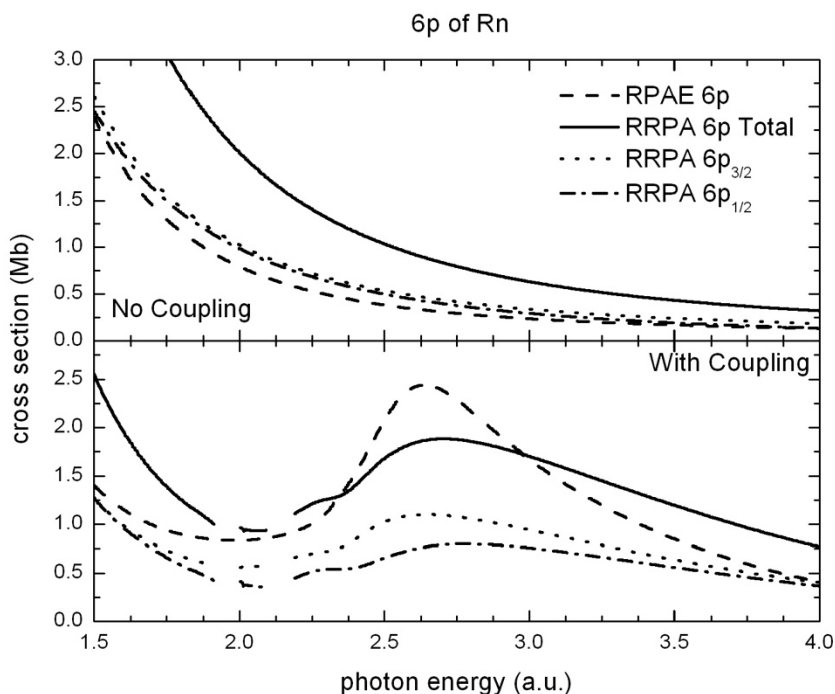


Figure 21: The partial photoionization cross section of 6p subshell of Rn, the top plot is without interchannel coupling included while the bottom one has the coupling included in the calculations. In both plots the dashed curve is the RPAE results and the dotted, dash-dot, and solid are the RRPA  $6p_{3/2}$ ,  $6p_{1/2}$ , and 6p total respectively.

Near the  $6p_{1/2}$  threshold in Figure 20, the RRPA  $6p_{1/2}$  cross section falls below the RRPA  $6p_{3/2}$  one; this is opposite of what was seen with the Rn 5p cross sections in Figure 13 at the opening of the  $5p_{1/2}$  subshell. In fact, both of the spin-orbit channels fall below the RPAE cross section, which wasn't the case in the 5p of radon (Figure 13). This brings the RRPA 6p total and RPAE cross sections more in line with each other. The inclusion of interchannel coupling doesn't affect the relative magnitudes or relations between the RPAE and RRPA cross sections. As photon energy increases, the dynamic effects push all of the RRPA cross sections above the RPAE, as seen in Figure 21, where the farther away from the threshold, the more pronounced the dynamic changes. These dynamic effects are diminished with the inclusion of interchannel coupling with the 5d cross sections. Just as for the 6s cross sections, interchannel coupling with the 5d cross

section greatly affects the 6p cross sections. Differences in the RPAE and RRPA cross sections are due to the differences in the 5d ones.

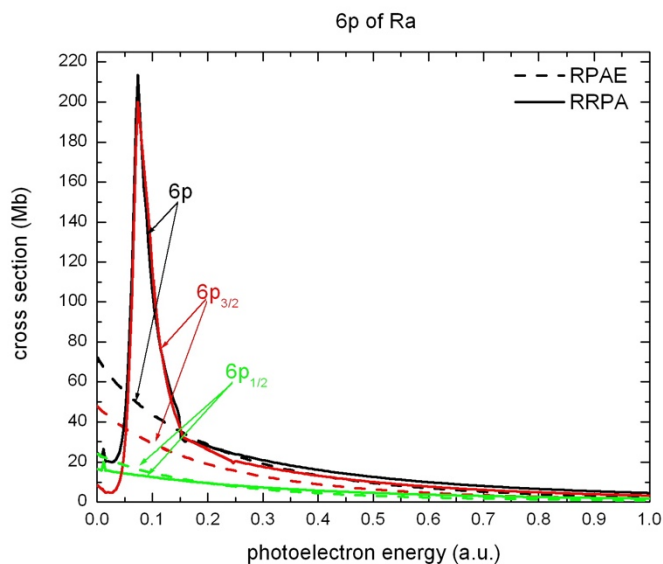


Figure 22: The partial photoionization cross section of the 6p subshell of Ra without interchannel coupling included in the calculation.

The solid curves are the results of the RRPA calculations while the dashed curves are the RPAE results. The RPAE  $6p_{3/2}$  and  $6p_{1/2}$  are produced by taking the normal RPAE result and multiplying by the corresponding branching ratios.

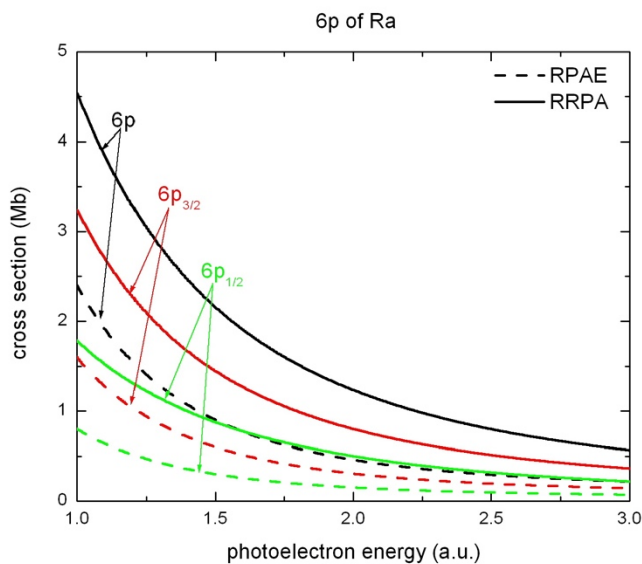


Figure 23: The partial photoionization cross section of the 6p subshell of Ra without interchannel coupling included in the calculation at higher energy.

The solid curves are the results of the RRPA calculations while the dashed curves are the RPAE results. The RPAE  $6p_{3/2}$  and  $6p_{1/2}$  are produced by taking the normal RPAE result and multiplying by the corresponding branching ratios.

Near the lowest energies of the plot in Figure 22, but below the autoionization resonance in the  $6p_{3/2}$  curve, there is a significant difference between the RRPA and RPAE  $6p_{3/2}$  results. This difference is corrected, *via* interchannel coupling, after the  $6p_{1/2}$  subshell opens up. This phenomenon will be seen to be more pronounced in the  $6p$  of nobelium. In the same region, the RRPA  $6p_{1/2}$  curve is lower than the RPAE  $6p_{1/2}$  results. Above the resonance region, the curves behave similarly to the radon case, Figure 18. This behavior continues as photoelectron energy increases, Figure 23.

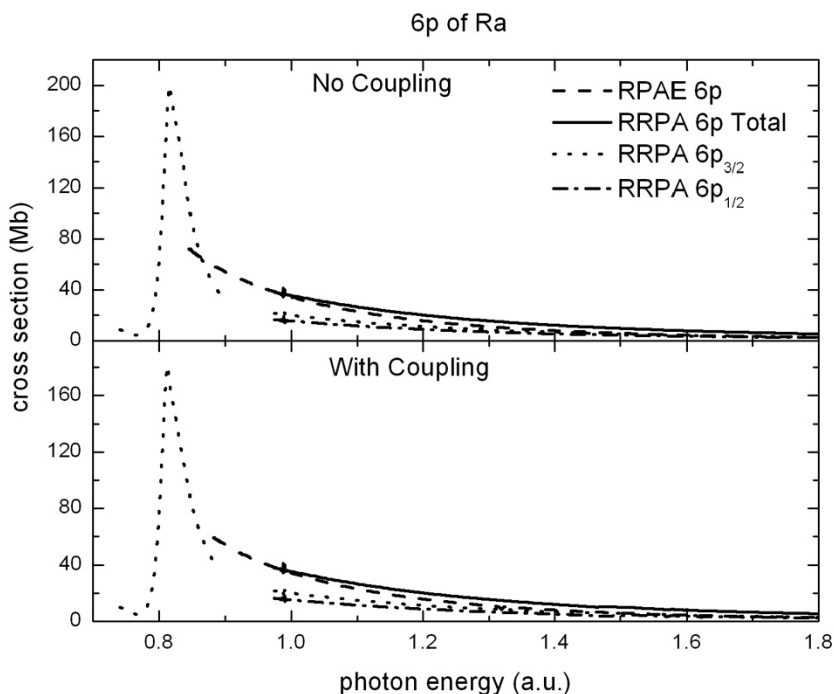


Figure 24: The partial photoionization cross section of  $6p$  subshell of Ra, the top plot is without interchannel coupling included while the bottom one has the coupling included in the calculations.

In both plots the dashed curve is the RPAE results and the dotted, dash-dot, and solid are the RRPA  $6p_{3/2}$ ,  $6p_{1/2}$ , and  $6p$  total respectively.

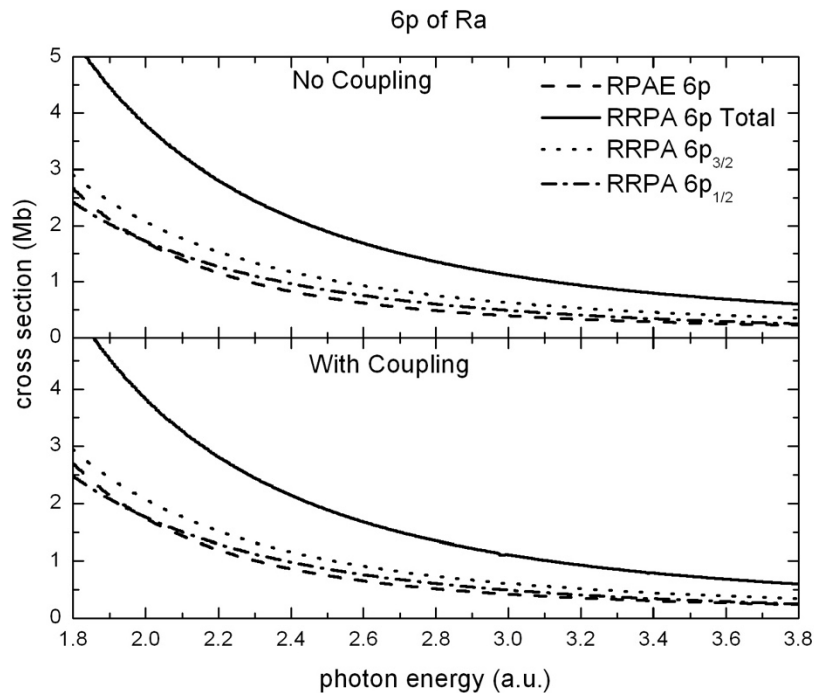


Figure 25: The partial photoionization cross section of 6p subshell of Ra, the top plot is without interchannel coupling included while the bottom one has the coupling included in the calculations. In both plots the dashed curve is the RPAE results and the dotted, dash-dot, and solid are the RRPA  $6p_{3/2}$ ,  $6p_{1/2}$ , and 6p total respectively.

Unlike in radon, the 5d of radium doesn't overshadow the 6p cross section. So the primary effect is still the dynamic changes that were present in Figures 22 and 23. These changes lower the cross section near the threshold and steadily increase it as photon energy increases.

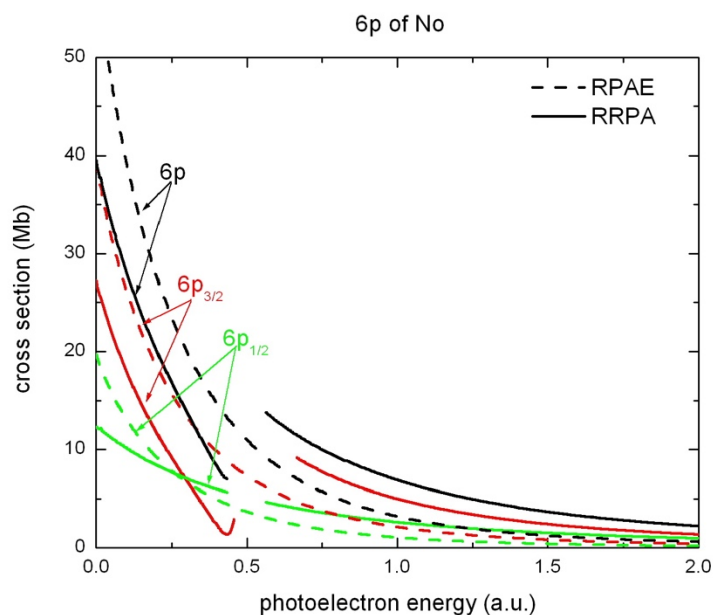


Figure 26: The partial photoionization cross section of the 6p subshell of No without interchannel coupling included in the calculation.

The solid curves are the results of the RRPA calculations while the dashed curves are the RPAE results. The RPAE  $6p_{3/2}$  and  $6p_{1/2}$  are produced by taking the normal RPAE result and multiplying by the corresponding branching ratios.

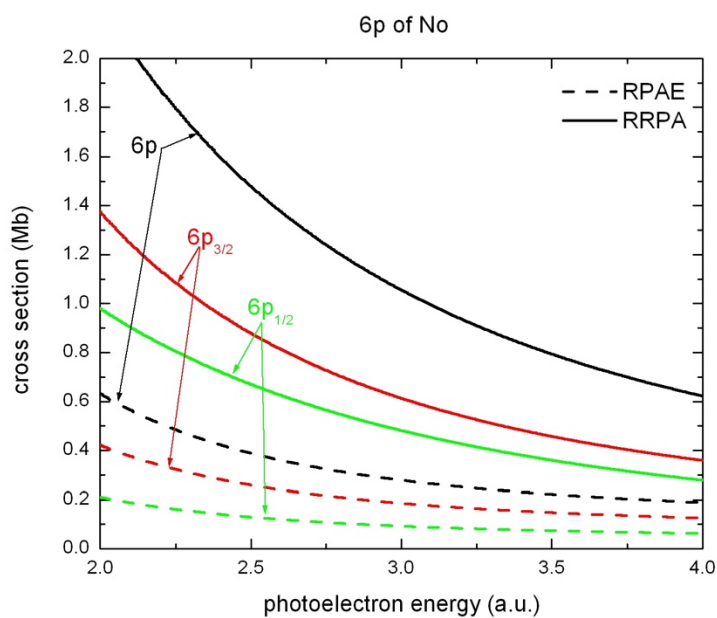


Figure 27: The partial photoionization cross section of the 6p subshell of No without interchannel coupling included in the calculation at higher energy.

The solid curves are the results of the RRPA calculations while the dashed curves are the RPAE results. The RPAE  $6p_{3/2}$  and  $6p_{1/2}$  are produced by taking the normal RPAE result and multiplying by the corresponding branching ratios.

In similar fashion to radium, dynamic effects diminish the No 6p cross sections near the threshold, but as photoelectron energy increases, dynamic effects amplify the cross sections.

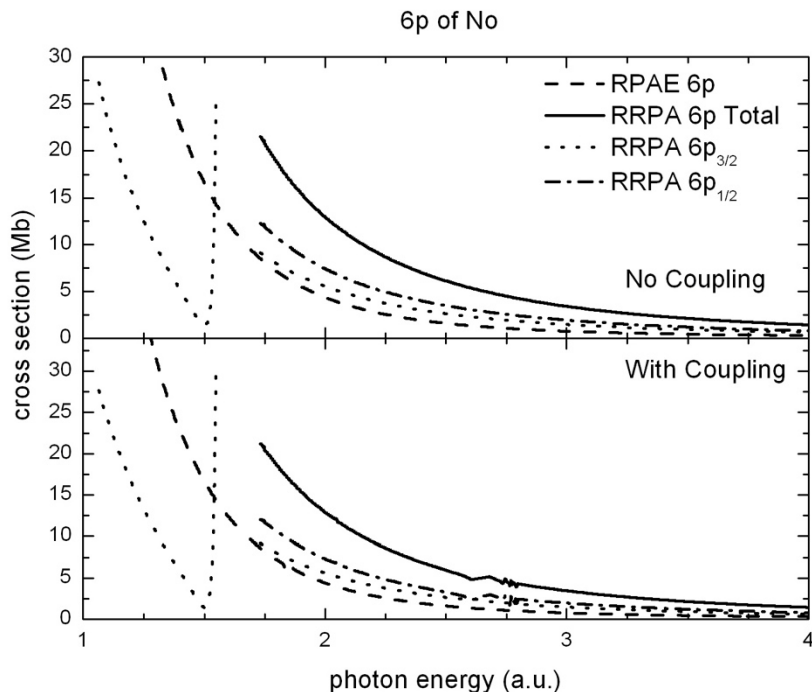


Figure 28: The partial photoionization cross section of 6p subshell of Ra, the top plot is without interchannel coupling included while the bottom one has the coupling included in the calculations. In both plots the dashed curve is the RPAE results and the dotted, dash-dot, and solid are the RRPA  $6p_{3/2}$ ,  $6p_{1/2}$ , and 6p total respectively.

Once again, with negligible effects from the 5d subshell *via* interchannel coupling, dynamic changes remain the prominent effect. Figure 28 for No shows behavior similar to Figures 24 and 25 for Ra. Of interest is the fact that at the  $6p_{1/2}$  threshold, the  $6p_{1/2}$  cross section is higher than the  $6p_{3/2}$  one. This is one of the few cases where the shift in thresholds doesn't diminish the dynamic effects. Just as in the  $6p_{3/2}$  of radium, there is a clear example of spin-orbit interchannel coupling, creating a significant change in the magnitude of the  $6p_{3/2}$  cross section above and

below the opening of the  $6p_{1/2}$  subshell. Spin-orbit interchannel coupling will be further explored in the 5d subshell section, where the effects are much more pronounced.

There is clear increase in the influence of relativistic effects on the  $np$  subshells as the nuclear charge increases. The relative difference between the RPAE thresholds and RRPA thresholds increases. In the 5p cases, the dynamic effects decreased as the nuclear charge increased, with No 5p being the outlier due to the nature of where the No 5p subshell is placed in the atom. But in the 6p cases there is no change in the dynamic effects as  $Z$  increases. The introduction of interchannel coupling in the 5p cases greatly alters the cross sections, with dynamic changes being diminished by both interchannel coupling and the shifts in thresholds., while in the 6p cases, dynamic changes are more prevalent and withstand the introduction of shifts and coupling, except for the 6p of radon, due to the magnitude of the 5d subshell and its effect on the surrounding subshells via interchannel coupling. In the 6p of radium and nobelium, there are observable effects of spin-orbit interchannel coupling, over and above the autoionization resonances, in the  $6p_{3/2}$  cross sections.

### 3.3 5d Subshell

The next inner most outer subshell is the 5d; Table 6 below presents the threshold of each of the elements in the case study. All of the energies are presented in atomic units (a.u.), and the DF\* column refers to the  $l - \frac{1}{2}$  ( $5d_{3/2}$ ) channel while the un-stared DF refers to the  $l + \frac{1}{2}$  ( $5d_{5/2}$ ) one.

Table 6: 5d Thresholds (a.u.)

Element	Hg	Rn	Ra	No
HF	0.71	2.33	3.30	6.48
DF	0.57	2.02	2.90	5.98
DF*	0.65	2.19	3.12	6.61

Once again, the difference between the un-starred DF and HF thresholds increases with increasing nuclear charge, like with the 5p case. Unlike the 5p case, the DF\* subshells are more bound than the HF subshells, except for nobelium, for similar reasons as the nobelium 5p. In this case, the un-starred DF exhibits the more dramatic differences between the un-starred DF and HF thresholds, when compared to the differences between the DF\* and HF thresholds.

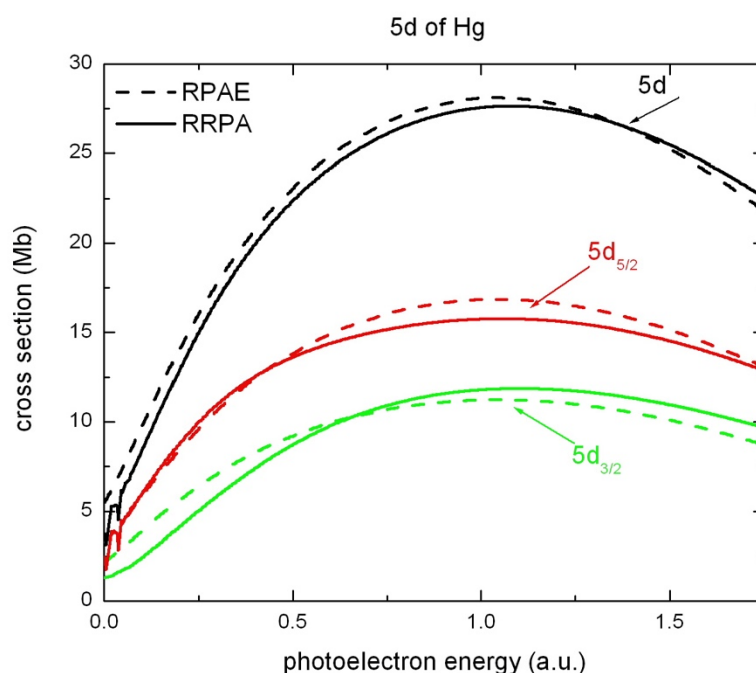


Figure 29: The partial photoionization cross section of the 5d subshell of Hg without interchannel coupling included in the calculation.

The solid curves are the results of the RRPA calculations while the dashed curves are the RPAE results. The RPAE  $5d_{5/2}$  and  $5d_{3/2}$  are produced by taking the normal RPAE result and multiplying by the corresponding branching ratios.

Dynamic effects are not as important as they were in the 5p cross section of mercury, but there are still hints of the  $j$  dependence of dynamic effects since the differences between the RPAE and RRPA  $5d_{5/2}$  and  $5d_{3/2}$  curves behave very differently than in the 5p cases. But these differences between the channels are not very significant. As such, the total 5d RRPA and RPAE cross

sections are practically identical for all intents and purposes. The kinks in the RRPA Total and RRPA  $5d_{5/2}$  curves are due to the resonances induced by the opening of the  $5d_{3/2}$  threshold.

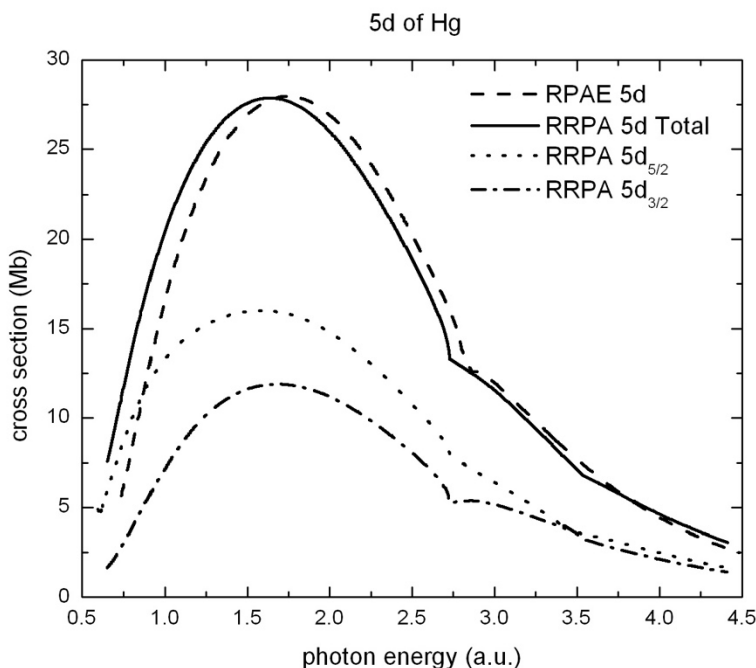


Figure 30: The partial photoionization cross section of 5d subshell of Hg. The dashed curve is the RPAE results and the dotted, dash-dot, and solid are the RRPA  $5d_{5/2}$ ,  $5d_{3/2}$ , and 5d total respectively.

As expected from the diminished dynamic effects, seen in Figure 29, the RRPA and RPAE cross sections are practically the same, just shifted to their respective thresholds. With the lack of significant dynamic effects, the lower of the spin-orbit channels,  $5d_{3/2}$ , is smaller than the  $5d_{5/2}$  cross section, which is expected as the  $5d_{5/2}$  subshell has two more electrons than the  $5d_{3/2}$  subshell. There are insignificant differences between calculations with and without interchannel coupling, so the uncoupled results have not been plotted. This is expected because, compared to the magnitudes of the nearby cross sections (6p and 6s), the 5d cross sections are much greater.

Therefore, the influence they have on the 5d in the form of interchannel coupling is almost nonexistent.

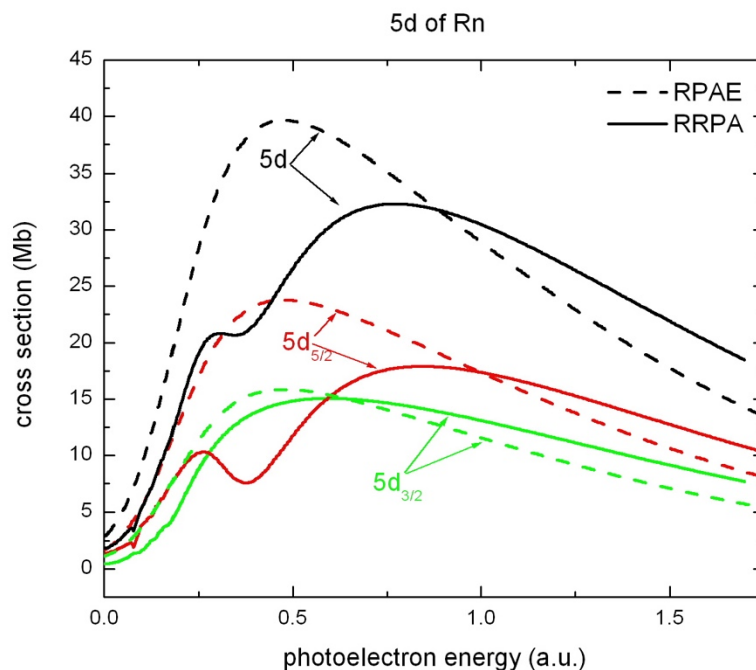


Figure 31: The partial photoionization cross section of the 5d subshell of Rn without interchannel coupling included in the calculation.

The solid curves are the results of the RRPA calculations while the dashed curves are the RPAE results. The RPAE  $5d_{5/2}$  and  $5d_{3/2}$  are produced by taking the normal RPAE result and multiplying by the corresponding branching ratios.

With all of the previous plots without interchannel coupling, it wasn't necessary to mention that interchannel coupling between the two spin-orbit channels remained in the calculations, because other than resonances in the upper channel due to the lower channel, there were no significant effects. With the 5d of radon, Figure 31, that doesn't remain the case; interchannel coupling between the two introduces a spin-orbit activated interchannel coupling resonance [30]. This complicates the investigation into the dynamics of this channel, except in the  $5d_{3/2}$  curves, where the behavior continues the pattern established in the 5p cases, as the nuclear charge increases so in turn do the dynamic effects. But the artificially produced RPAE  $5d_{5/2}$  curve accurately creates

the  $5d_{5/2}$  cross section if interchannel coupling with the  $5d_{3/2}$  channel is removed, with similar comparisons being drawn from the RPAE and RRPA total cross sections.

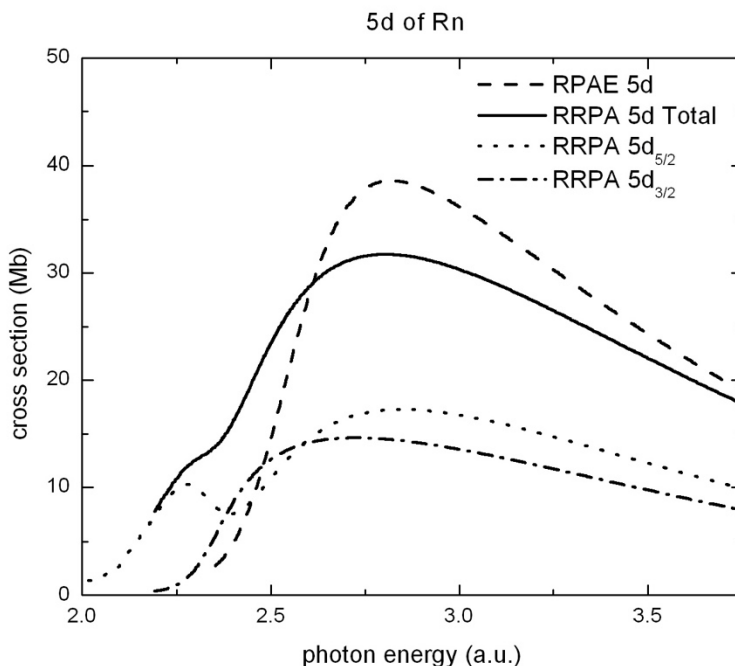


Figure 32: The partial photoionization cross section of 5d subshell of Rn, the top plot is without interchannel coupling included while the bottom one has the coupling included in the calculations. In both plots the dashed curve is the RPAE results and the dotted, dash-dot, and solid are the RRPA  $5d_{5/2}$ ,  $5d_{3/2}$ , and 5d total respectively.

The shifting of thresholds diminishes the spin-orbit activated resonances in the RRPA Rn 5d total cross section, seen in Figure 32, from what it was in Figure 31. Just as in the 5p cases, the shifting of threshold reduces the influence of the dynamic effects. For the same reasons as the mercury 5d, the introduction of interchannel coupling with 6s has little, or no effect on the cross section.

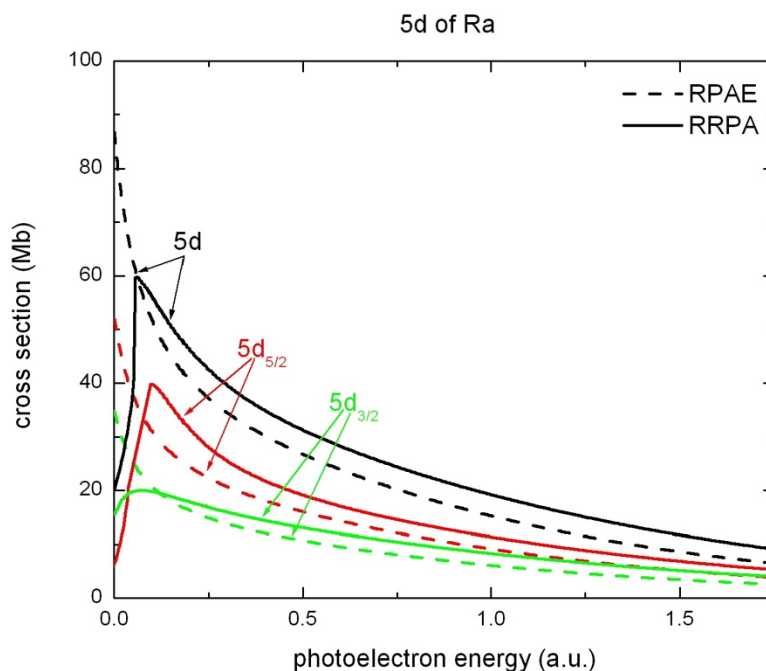


Figure 33: The partial photoionization cross section of the 5d subshell of Ra without interchannel coupling included in the calculation.

The solid curves are the results of the RRPA calculations while the dashed curves are the RPAE results. The RPAE  $5d_{5/2}$  and  $5d_{3/2}$  are produced by taking the normal RPAE result and multiplying by the corresponding branching ratios.

With most of the giant  $d$  resonance falling into the discrete part of the spectrum of the Ra 5d RRPA curves, the chances of a spin-orbit activated resonance occurring in the continuum is diminished. All of the resonance in the RPAE cross section has fallen into the discrete, which causes most dramatic difference between the RPAE and RRPA curves. Other than that, Figure 33 shows similar results to that of mercury 5d, Figure 29. As was seen in Figure 33, the resonance has fallen into the discrete spectrum. Shifting the thresholds back into place, once again diminishes the dynamic effects, as seen in Figure 34.

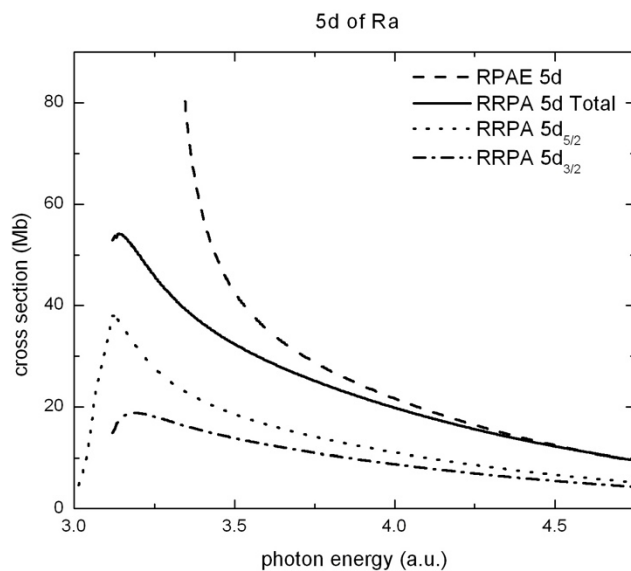


Figure 34: The partial photoionization cross section of 5d subshell of Ra, the top plot is without interchannel coupling included while the bottom one has the coupling included in the calculations. In both plots the dashed curve is the RPAE results and the dotted, dash-dot, and solid are the RRPA  $5d_{5/2}$ ,  $5d_{3/2}$ , and 5d total respectively.

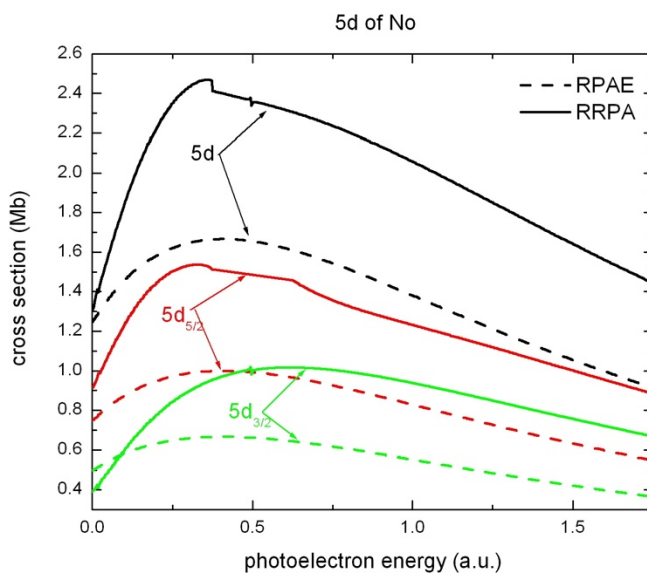


Figure 35: The partial photoionization cross section of the 5d subshell of No without interchannel coupling included in the calculation. The solid curves are the results of the RRPA calculations while the dashed curves are the RPAE results. The RPAE  $5d_{5/2}$  and  $5d_{3/2}$  are produced by taking the normal RPAE result and multiplying by the corresponding branching ratios.

Figure 35, showing the 5d of No, is the first 5d case where dynamic effects become very significant. The RRPA  $5d_{5/2}$  (solid) curve is comparable to the RPAE total (dashed) curve, similar to the mercury and radon 5p cross sections, Figures 10 and 12. The trend of the dynamic effects is the opposite of what it was in the 5p cross sections. The kink in the RRPA total and  $5d_{5/2}$  is due to the removal of the resonances due to the opening of the  $5d_{3/2}$  channel.

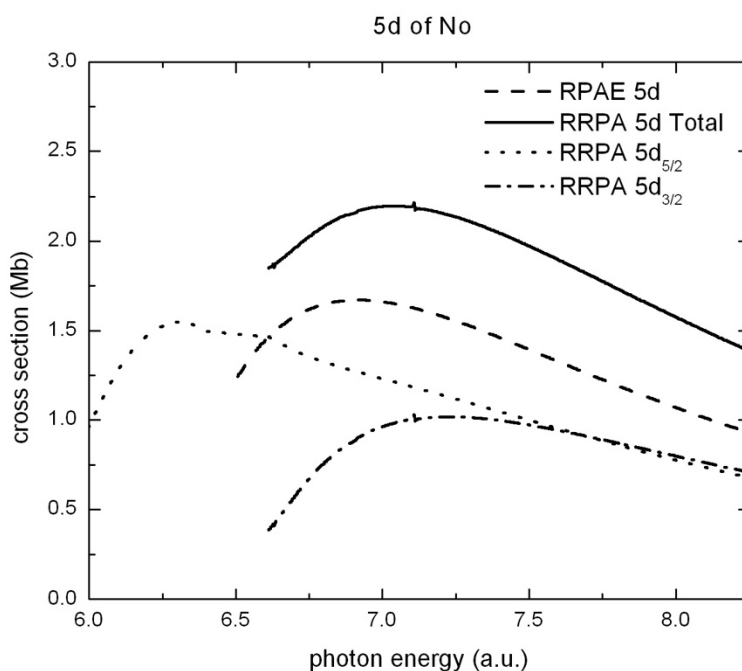


Figure 36: The partial photoionization cross section of 5d subshell of No, the top plot is without interchannel coupling included while the bottom one has the coupling included in the calculations. In both plots the dashed curve is the RPAE results and the dotted, dash-dot, and solid are the RRPA  $5d_{5/2}$ ,  $5d_{3/2}$ , and 5d total respectively.

Even though the shifting of threshold diminishes the effects of the dynamics, because of how significant they are, they are still present in Figure 36, which shows up in the fact that the RRPA total and the RPAE are qualitatively the same, but differ quantitatively. Of interest in Figure 36, above  $7.75 a.u.$ , the RRPA  $5d_{3/2}$  cross section is equal to the RRPA  $5d_{5/2}$  one and larger than the  $5d_{5/2}$  at higher energy. Due to the sheer magnitude of the 5d shape resonance, interchannel

coupling of outside channels has negligible effects on the cross sections of the 5d subshells.

Dynamic effects increase as the nuclear charge increases, which is the reverse of what happened in the 5p cases.

### 3.4 Confined Atoms

Fullerenes are hollow cages of carbon atoms that are formed when carbon condenses. Confined atoms are atoms trapped inside hollow cages whose sizes are commensurable with the sizes of atoms. We use fullerenes as the hollow cages. When an atom A is inside the  $C_{60}$  cage this produces a state of matter called an endohedral fullerene,  $A@C_{60}$ .

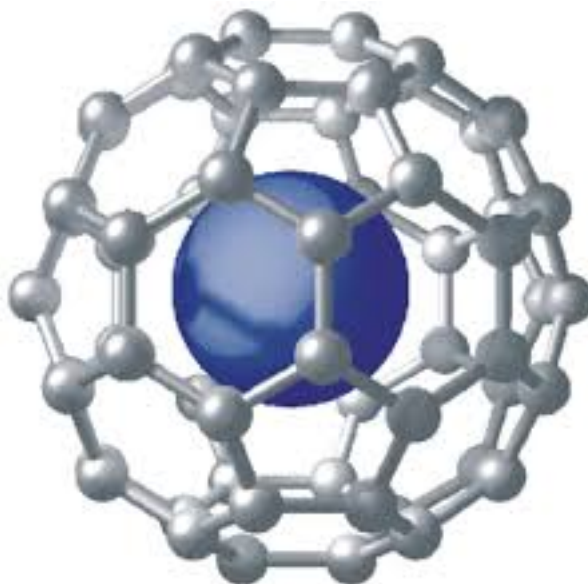


Figure 37:  $A@C_{60}$

Endohedral  $C_{60}$  molecules can be prepared by a “brute force” method [31], where ions of atoms are accelerated and implanted into the  $C_{60}$  cage. The ions need enough energy to open up the cage and enter. Once inside, the atom is shielded from outside atoms maintaining its isolated atomic structure. The photoionization cross section of atoms confined within  $C_{60}$  cages have been topical subjects of theory for some years now [32]. These investigations have shown strong

resonances in the photoionization cross sections of endohedrally confined atoms brought about by the presence of the confining shell, they have been termed confinement resonances. [33] The  $C_{60}$  was chosen because it is nearly spherical which allows us to greatly simplify the calculations; utilizing this symmetry the potential  $V_c(r)$  can be modeled [32, 33] using a finite spherical well potential where the dimensions are  $r_{in} = 5.8 \text{ a.u.}$  as the inner radius,  $\Delta = 1.9 \text{ a.u.}$  as the width of the confining potential, and  $V_o = 0.302 \text{ a.u.}$  as the depth of the confining potential,

$$V_c(r) = -V_o, r_{in} \leq r \leq r_{in} + \Delta; = 0, \text{ otherwise.}$$

The effects of the  $C_{60}$  potential modeled by a static spherical well is reasonable since in most of the cases we are dealing with the energy region well above the  $C_{60}$  plasmons [32, 33]. For surfaces and bulk matter, i.e., extended systems, plasmons, or other “quasi-particles,” are used to describe collective phenomena induced by electron correlations [34]. Such a model, for example, produced reasonably accurate photoionization cross sections for the confinement resonances associated with the photoionization of Xe 4d [35]; furthermore, it has been shown that the existence of discontinuities in the potential, inherent in a spherical square well, have no substantial impact on the resulting photoionization cross sections [36]. Just as with free atoms, interchannel coupling can revive confinement resonances in outer subshells far above their thresholds near inner subshells’ thresholds [37]. Given this understanding of interchannel coupling effects on confinement resonances we are lead to investigate the effects of spin-orbit activated interchannel coupling on them. This investigation is of importance, in that ordinary confinement resonances contain information of the geometry of the confining cage [38, 39], but the interchannel coupling would obviate the simple geometric interpretation. And, of importance, virtually all subshells of confined atoms exhibit near-threshold confinement

resonances [32,33,37, 40]. Just as in the free cases, there are indeed structures induced in the cross sections of confined atoms due to spin-orbit activated interchannel coupling; these structures have been termed spin-orbit activated confinement resonances [30]. It is important to reiterate the point that there, in most cases are no near-threshold shape resonances in the free atom. And, owing to the nature of the angular momentum barrier which causes these resonances in free atoms [15, 41], such resonances are relatively rare in np subshells of free atoms [42]. However, as implied above, near-threshold confinement resonances for subshells of all angular momenta are ubiquitous in confined atoms [32, 33]. This means that spin-orbit induced interchannel coupling resonances, which are rare in free atoms, will be a very general phenomenon in confined atoms. Spin-orbit activated confinement resonances are just one example of how relativity can obscure the simple geometric interpretation of confinement resonances. Some of the others will be discussed below. Rather than examine the evolution of these changes as the nuclear charge increases like what was done in the free atom results, the results will be grouped together based on the cause of the relativistic changes.

### 3.5 Threshold Shifts

The act of confining any atom in a C<sub>60</sub> fullerene screens the confined atom from outer influences. In addition, the added attractive potential causes all of the subshells to become more bound, thus shifting their respective thresholds.

Table 7: Confined Thresholds (a.u.)

	Free	Confined	Shift
Hg HF	0.71	0.81	0.10
Hg DF	0.57	0.63	0.05
Hg DF*	0.65	0.70	0.05
Rn HF	2.33	2.36	0.03
Rn DF	2.02	2.05	0.03
Rn DF*	2.19	2.22	0.03
Ra HF	3.30	3.35	0.05
Ra DF	2.90	2.99	0.09
Ra DF*	3.12	3.20	0.08

Table 7 shows the respective thresholds in the 5d subshells of mercury, radon, and radium to illustrate the shifts in thresholds due to confinement. All of the energies are presented in atomic units (a.u.). The un-starred DF is the  $5d_{5/2}$  and the starred is the  $5d_{3/2}$ . The “Shift” column is the difference between the confined and free thresholds. Clearly the confined cases are more bound, but what is interesting is that in mercury and radium the shifts are different for HF and DF. This is a common occurrence throughout the other subshells. One would expect that with the same confining potential the shifts in thresholds would be the same in both models. For that to be the case the subshells’ wavefunctions would have to be in the same positions. Due to dynamic changes the DF wavefunctions are in different positions, so they experience the confinement potential slightly differently, which translates to the different shifts in the two models. In the radon case, the dynamic changes do not affect the wavefunctions enough to alter the shifts in thresholds due to confinement.

### 3.6 Relativistic Confinement Resonances

The existence of the spin-orbit doublet subshells is responsible for the most direct change to confinement resonances due to relativity; because confinement resonances are due to the confining cage, they are dependent upon photoelectron energy rather than photon energy. When looking at the, for example, the  $5p_{3/2}$  and  $5p_{1/2}$  cross sections of radium, both of the doublets have the same near threshold resonance structure, Figure 38. Both of these near-threshold resonance structures match the non-relativistic near-threshold resonance structure, which is to be expected.

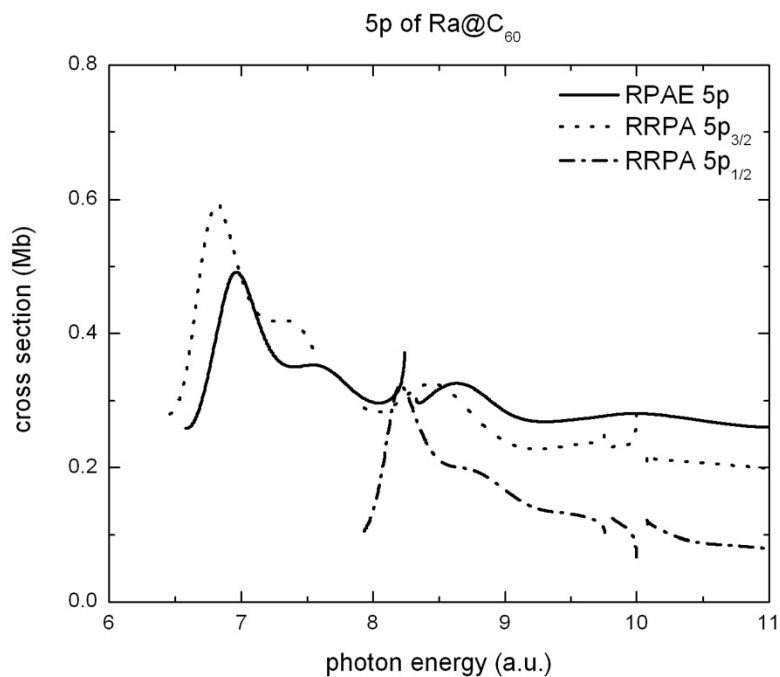


Figure 38: The partial photoionization cross section of the 5p subshell of @Ra. With the RPAE 5p being plotted with a solid line, and the RRPA  $5p_{3/2}$  and  $5p_{1/2}$  with dotted and dash-dot respectively. Interchannel coupling has been included, the gaps are the omitted resonance regions.

Although this isn't the focus of Figure 38, the dynamic behavior matches that of the free cross section, Figure 15, implying that confinement has no effect on the dynamic effects. Now where the alteration to the behavior of the confinement resonances comes into play is when viewing RRPA 5p total cross section ( $5p_{3/2} + 5p_{1/2}$ ). Owing to the difference in thresholds between the doublet subshells, the near threshold resonance structure is repeated at the opening of the  $5p_{1/2}$  threshold, Figure 39.

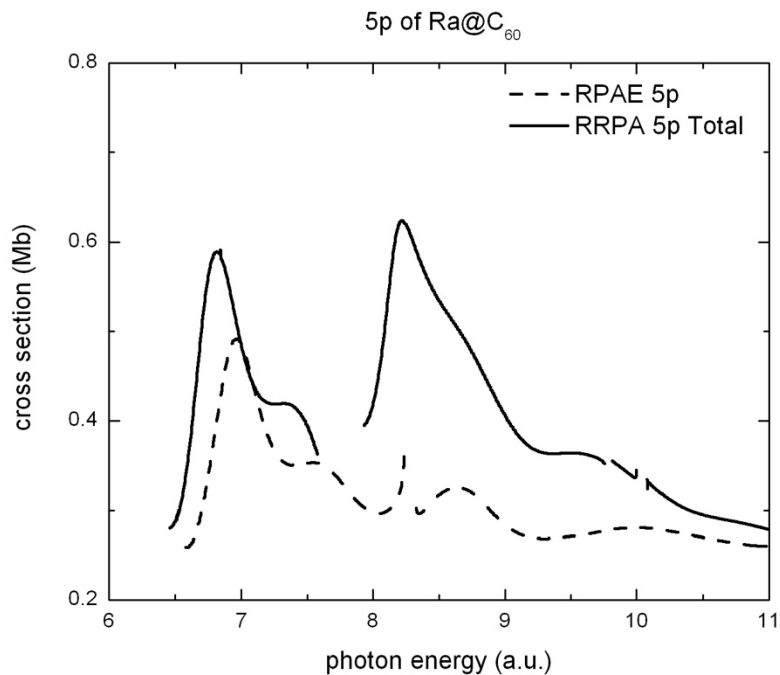


Figure 39: The partial photoionization cross section of the total 5p subshells of @Ra. With the RPAE 5p being plotted with dashed, and the RRPA 5p total with solid. Interchannel coupling has been included, the gaps are the omitted resonance regions.

Clearly present is a repeated near-threshold resonance structure, but with slight differences.

These differences are due to the misalignment of confinement resonances between the two doublet subshells. This can be seen in the flattening of the second resonance in the repeated near threshold structure at the opening of the  $5p_{1/2}$  threshold. This phenomenon is present in all of the subshells with spin-orbit doublets, i.e., all subshells except the  $ns$  subshells.

### 3.7 Confinement-Affected Spin-Orbit Resonances

Although there are fewer cases of free atoms with spin-orbit activated interchannel coupling resonances than confined atoms with spin-orbit activated confinement resonances, it is still important to remark on how spin-orbit activated interchannel coupling resonances are affected by the confinement.

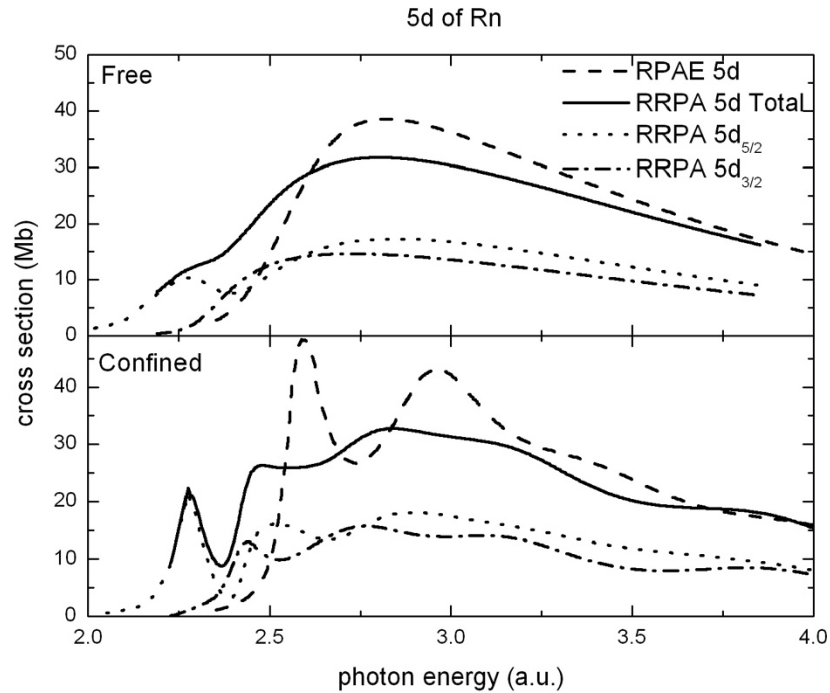


Figure 40: The partial photoionization of the 5d subshell of both free and confined Rn, with the free case being the top plot and the confined at the bottom.

In both plots the RPAE 5d results are plotted with dashed lines, while the RRPA  $5d_{5/2}$ ,  $5d_{3/2}$ , and 5d total are plotted in dotted, dash-dot, and solid lines respectively.

Recall that the  $5d_{5/2}$  subshell cross section has a spin-orbit activated interchannel coupling resonance due to the  $5d_{3/2}$  subshell, as seen in the top plot of Figure 40. Once confined, the additional resonance greatly affects the cross section, making the RPAE and RRPA cross sections completely different. In order to study the extent of these changes, it is helpful to perform calculations of the confined 5d subshells without coupling between the two doublet subshells, and the results of these uncoupled calculations are shown in Figure 41.

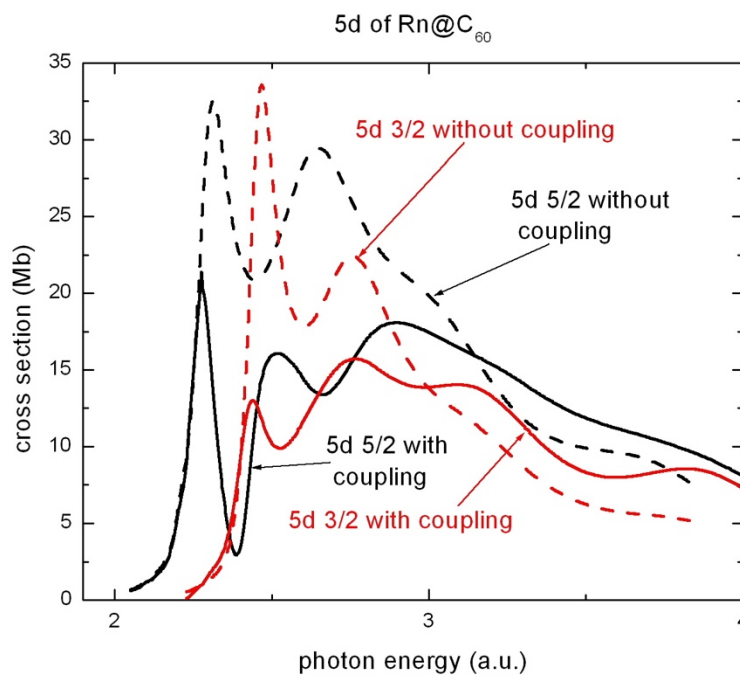


Figure 41: The partial photoionization cross section of the 5d spin-orbit doublet subshells of Rn. Where the solid curves include coupling between the subshells, and the dashed curves do not. The  $5d_{5/2}$  results are plotted in black, and the  $5d_{3/2}$  results are plotted in red.

Without interchannel coupling between the two 5d spin-orbit doublet subshells, both of their cross sections resemble the non-relativistic 5d cross section, seen in Figure 40. The spin-orbit activated interchannel coupling resonance in the free cross section of radon produces an extra major resonance in the confined 5d cross section. Interestingly the  $5d_{5/2}$  cross section isn't the only subshell that is affected by the spin-orbit activated interchannel coupling resonance, in Figure 41. There is clear alteration to the  $5d_{3/2}$  cross section as well. This phenomenon is only possible if the free atom already has a spin-orbit activated interchannel coupling resonance. But, as stated previously, it is possible for confinement resonances to create these spin-orbit activated interchannel coupling resonances, termed spin-orbit confinement resonances. The idea behind these spin-orbit confinement resonances is the same as the spin-orbit activated interchannel

coupling resonances, but their origin lies in the behavior of near threshold confinement resonances.

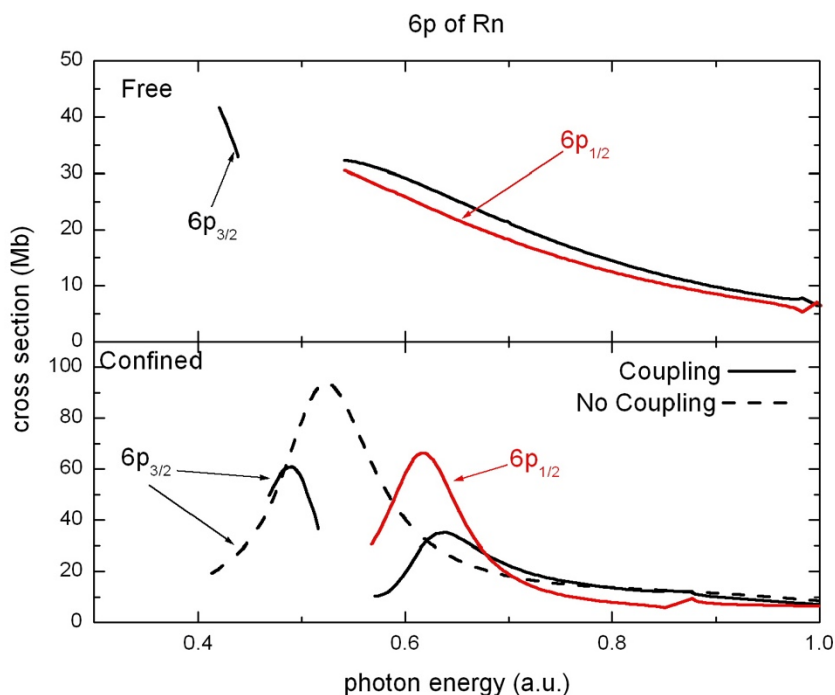


Figure 42: The partial photoionization of the 6p subshell of both free and confined Rn, with the free case being the top plot and the confined at the bottom.

In both plots the RRPAs  $6p_{3/2}$  and  $6p_{1/2}$  are plotted in black and red respectively. In the bottom plot the dashed curve has coupling removed, while the solid curve has coupling intact.

In the bottom plot of Figure 42, there is clear evidence of a near threshold confinement resonance. And just as in the 5d subshell cross section, there is an extra resonance present in the  $6p_{3/2}$  cross section, that if it was a normal near-threshold confinement resonance, it would appear in the non-relativistic and  $6p_{1/2}$  cross sections as well. Once again, to investigate this phenomenon, calculations are performed removing the interchannel coupling between the relativistic 6p subshells. For clarity, the autoionization resonances in the  $6p_{3/2}$  cross section due to the opening of the  $6p_{1/2}$  subshell have been removed. With the exclusion of interchannel

coupling, it became apparent that the second major resonance in the  $6p_{3/2}$  is in fact a spin-orbit confinement resonance.

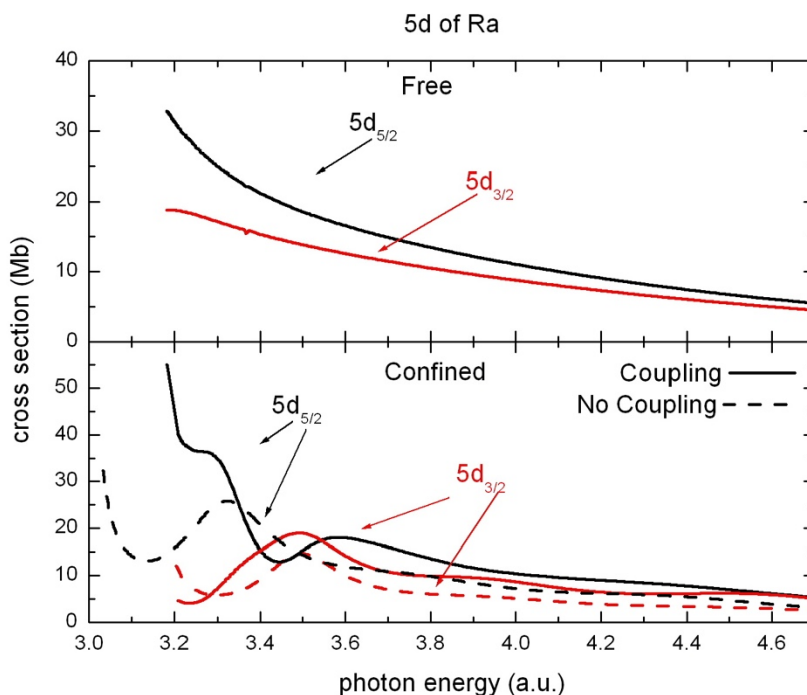


Figure 43: The partial photoionization of the  $6p$  subshell of both free and confined Ra, with the free case being the top plot and the confined at the bottom.

In both plots the RRPA  $6p_{3/2}$  and  $6p_{1/2}$  are plotted in black and red respectively. In the bottom plot the dashed curve has coupling removed, while the solid curve has coupling intact.

Figure 43 shows the same situation except it is in the  $5d$  subshell of radium. But in this case, there are slight alterations to the  $5d_{3/2}$  cross section due to the  $5d_{5/2}$  subshell, which wasn't really the case in the  $6p$  of radon, Figure 42.

As stated several times, the most important change induced by relativity is the alteration of confinement resonances, which obscures the information about the confining structure contained in the confinement resonances. Currently work is proceeding on  $\text{No}@C_{60}$  for completeness, and to investigate if there are any more significant changes to the confinement resonances with greater relativistic effects.

## 4 CONCLUSION

Naturally the obvious conclusion that can be made about the evolution of relativistic effects is that they increase with the atomic number. But that isn't necessarily the full story, as can be seen with the decreasing dynamic effects in the 5p cross sections in the free atoms. At first this appears to be counterintuitive, but is an example of indirect relativistic effects. With the introduction of relativity, there are significant changes to the photoionization cross section that can't be ignored, whether indirect, as in the 5p example, or direct effects such as removal of the Cooper Minima in the *ns* cross sections, dynamic effects, and spin-orbit activated interchannel coupling. In most of the cases examined, once interchannel coupling is introduced into the calculation, the obvious changes due to relativistic effects are diminished. But this does lead to another example of an indirect relativistic effect (see the radon cross sections with coupling with the Rn 5d subshells, where relativistic effects are induced in other partial cross sections via interchannel coupling.) Due to the nature of the near-threshold confinement resonances, confined atoms are perfect systems to study spin-orbit activated interchannel coupling between spin-orbit doublets. Naturally the next step in this investigation is to probe further into the inner subshells of our test cases, in order to further explore the importance of relativistic effects. During the study of relativistic dynamic effects, we discovered that the branching ratios of spin-orbit doublet subshells are more sensitive to dynamic effects. Even for relatively light elements, a study of dynamic effects using this lens is also being put together. And since these effects can be seen in lighter elements, experiments can be performed to help establish the importance of these dynamic effects. Over the course of the last couple of years, a new area of study in atomic photoionization has emerged, time delay. It would be important to understand how relativity effects the photoionization time delay, which is currently being scrutinized.

## REFERENCES

- [1] P. A. M. Dirac, Proc. R. Soc. A **117**, 778. (1928)
- [2] E. J. Baerends et al, J. Phys. B **23**, 3225 (1990)
- [3] J. P. Desclaux and Yong-Ki Kim, J. Phys. B **8**, 1177 (1975)
- [4] A. F. Starace, (1982) *Theory of Atomic Photoionization*. Berlin, Heidelberg: Springer-Verlag
- [5] J. J. Sakura, (1967) *Advanced Quantum Mechanics*. Reading, Mass: Addison-Wesley Publishing Co.
- [6] L. D. Landau and E. M. Lifshitz, (1965) *Quantum Mechanics, 2<sup>nd</sup> edn*. Oxford: Pergamon Press
- [7] J. A. R. Samson, Adv. At. Mol. Phys. **2**, 117 (1966)
- [8] A. Dalgarno and G. A. Victor, Proc. R. Soc. A **291**, 291 (1966).
- [9] W. R. Johnson and C. D. Lin, Phys. Rev. A **20** 3 (1979)
- [10] M. Ya. Amusia and N. A. Cherepkov, Case Stud. At. Phys. **5**, 47 (1975)
- [11] M. Ya. Amusia and L. V. Chernysheva, (1997) *Computation of Atomic Processes*. Philadelphia, Pennsylvania: IOP Publishing
- [12] L. Labzowsky, G. Klimchitskaya, and Yu Dmitriev, (1993) *Relativistic Effects in the Spectra of Atomic Systems*. Philadelphia, Pennsylvania: IOP Publishing
- [13] J. W. Cooper, Phys. Rev. **128**, 681 (1962)
- [14] J. W. Cooper, Phys. Rev. Lett. **13**, 762 (1964)
- [15] S.T. Manson and J. W. Cooper, Phys. Rev. **165**, 126 (1968)
- [16] S. T. Manson, Phy Rev A **31**, 3698 (1985)
- [17] D. L. Hansen, O. Hemmers, H. Wang, D. W. Lindle, I. A. Sellin, H. S. Chakraborty, P. C. Deshmukh, and S. T. Manson, Phys. Rev. A **60**, R2641 (1999)

- [18] H. S Chakraborty, P. C. Deshmukh and S. T. Manson, *Astrophysical Journal* **595**, 1307 (2003).
- [19] H. Wang, G. Snell, O. Hemmers, M. M. Sant'Anna, I. Sellin, N. Berrah, D. W. Lindle, P. C. Deshmukh, N. Haque and S. T. Manson, *Phys. Rev. Letters* **87**, 123004 (2001).
- [20] A. Kivimäki, U. Hergenhahn, B. Kempgens, R. Hentges, M. N. Piancastelli, K. Maier, A. Ruedel, J. J. Tulkki, and A. M. Bradshaw, *Phys. Rev. A* **63**, 012716 (2000)
- [21] M. Ya. Amusia, L. V. Chernysheva, S. T. Manson, A. M. Msezane, and V. Radojević, *Phys. Rev. Lett.* **88**, 093002 (2002)
- [22] M. Ya. Amusia, A. S. Baltentkov, L. V. Chernysheva, Z. Felfli, A. Z. Msezane and S. T. Manson, *J. Phys. B* **37**, 937 (2004)
- [23] S. Sunil Kumar, T. Banerjee, P. C. Deshmukh and S. T. Manson, *Phys. Rev A* **79**, 043401 (2009)
- [24] T. Richter, E. Heinecke, P. Zimmermann, K. Godehusen, M. Yalçinkaya, D. Cubaynes, and M. Meyer, *Phys. Rev. Lett.* **98**, 143002 (2007)
- [25] H Farrokhpour, M Alagia, M Ya Amusia, L Avaldi, L V Chernysheva, M Coreno, M de Simone, R Richter, S Stranges and M Tabrizchi, *J. Phys. B* **39**, 765 (2006)
- [26] V. Radojević, D. M. Davidović, and M. Ya. Amusia, *Phys. Rev. A* **67**, 022719 (2003)
- [27] M. Ya. Amusia, N. A. Cherepkov, L. V. Chernysheva, Z. Felfli, and A. Z. Msezane, *J. Phys. B* **38**, 1133 (2005)
- [28] M. Ya. Amusia, L. V. Chernysheva, Z. Felfli, and A. Z. Msezane, *Phys. Rev. A* **73**, 062716 (2006)
- [29] T. E. H. Walker and J. T. Waber, *J. Phys. B* **7** 674 (1974)
- [30] D. A. Keating, et al, *J. Phys. B* **50** 175001 (2017)

- [31] H. Shinohara 2000 Rep. Prog. Phys. **63**, 843
- [32] V. K. Dolmatov 2009 Adv. Quant. Chem. **58**, 13
- [33] V. K. Dolmatov, A. S. Baletenkov, J. P. Connerade and S. T. Manson, 2004 Radiat. Phys. Chem., **70**, 417.
- [34] Mohamed E. Madjet et al, J. Phys. B **41** 105101 (2008)
- [35] R. A. Phaneuf, A. L. D. Kilcoyne, N. B. Aryal, K. K. Baral, D. A. Esteves-Macaluso, C. M. Thomas, J. Hellhund, R. Lomsadze, T. W. Gorczyca, C. P. Ballance, S. T. Manson, M. F. Hasoğlu, S. Schippers, and A. Müller, Phys. Rev. A **88**, 053402 (2013).
- [36] V. K. Dolmatov, J. L. King and J. C. Oglesby, J. Phys. B **45**, 105102 (2012).
- [37] V. K. Dolmatov, G. Craven, E. Guler, and D. Keating, Phys. Rev. A **80**, 035401(2009).
- [38] J. P. Connerade, V. K. Dolmatov and S. T. Manson, J. Phys B **33**, 2279 (2000).
- [39] A. Potter, M. A. McCune, R. De, M. E. Madjet and H. S. Chakraborty, Phys. Rev. A **82**, 033201 (2010) and references therein.
- [40] M. J. Puska and R. M. Nieminen, Phys. Rev. A **47**, 1181 (1993).
- [41] A. R. P. Rau and U. Fano, Phys. Rev. **167**, 7 (1968).
- [42] V. Schmidt, Rep. Prog. Phys. **55**, 1483 (1992) and references therein.